

12

AD-A149 475

Final Report
Carbon Vaporization Condensation Effects

R. L. BAKER and J. M. McDONOUGH
Vehicle Engineering Division

and

K. C. HERR, R. A. KLINGBERG, and J. C. COFFER
Aerophysics Laboratory
The Aerospace Corporation
El Segundo, CA 90245

and

M. A. COVINGTON
NASA Ames Research Center
Moffett Field, CA 94035

31 July 1984

APPROVED FOR PUBLIC RELEASE;
DISTRIBUTION UNLIMITED

Prepared for
OFFICE OF NAVAL RESEARCH
Arlington, VA 22217
SPACE DIVISION
AIR FORCE SYSTEMS COMMAND
Los Angeles Air Force Station
P.O. Box 92960, Worldway Postal Center
Los Angeles, CA 90009-2960

DTIC
ELECTE
JAN 15 1985
S D
E

85 01 08 051

DTIC FILE COPY

This final report was prepared for the Office of Naval Research, Arlington, VA 22217, by The Aerospace Corporation, El Segundo, CA 90245, under Contract No. F04701-82-C-0083 with the Space Division, Air Force Systems Command, P.O. Box 92960, Worldway Postal Center, Los Angeles, CA 90009. It was reviewed and approved for The Aerospace Corporation by E.G. Hertler, Principal Director, Aero Engineering Subdivision.

This report has been reviewed by the Public Affairs Office (PAS) and is releasable to the National Technical Information Service (NTIS). At NTIS, it will be available to the general public, including foreign nations.

This technical report has been reviewed and is approved for publication. Publication of this report does not constitute Air Force approval of the report's findings or conclusions. It is published only for the exchange and stimulation of ideas.

24 Oct. 1984

for Paul C. Bisler
Gerhard E. Aichinger
Technical Advisor

FOR THE COMMANDER

James A. Bornino
James A. Bornino
Chief, Aerospace Contract Management Office

UNCLASSIFIED

SECURITY CLASSIFICATION OF THIS PAGE (When Data Entered)

REPORT DOCUMENTATION PAGE		READ INSTRUCTIONS BEFORE COMPLETING FORM
1. REPORT NUMBER SD-TR-84- 53	2. GOVT ACCESSION NO. AD-A149 475	3. RECIPIENT'S CATALOG NUMBER
4. TITLE (and Subtitle) CARBON VAPORIZATION/CONDENSATION EFFECTS		5. TYPE OF REPORT & PERIOD COVERED Final Report June 1979-Sept. 1983
		6. PERFORMING ORG. REPORT NUMBER TR-0084(9975)-3
7. AUTHOR(s) R.L. Baker, J.M. McDonough, K.C. Herr, R.A. Klingberg, J.C. Coffey--The Aerospace Corp. M.A. Covington, NASA Ames Research Center		8. CONTRACT OR GRANT NUMBER(s) F04701-83-C-0084
9. PERFORMING ORGANIZATION NAME AND ADDRESS The Aerospace Corporation El Segundo, California 90245		10. PROGRAM ELEMENT, PROJECT, TASK AREA & WORK UNIT NUMBERS
11. CONTROLLING OFFICE NAME AND ADDRESS Office of Naval Research Eastern/Central Regional Office Boston, MA 02210		12. REPORT DATE 31 July 1984
14. MONITORING AGENCY NAME & ADDRESS (if different from Controlling Office) Space Division Los Angeles Air Force Station Los Angeles, CA 90009		13. NUMBER OF PAGES 77
		15. SECURITY CLASS. (of this report) Unclassified
		15a. DECLASSIFICATION/DOWNGRADING SCHEDULE
16. DISTRIBUTION STATEMENT (of this Report) Approved for public release; distribution unlimited		
17. DISTRIBUTION STATEMENT (of the abstract entered in Block 20, if different from Report)		
18. SUPPLEMENTARY NOTES		
19. KEY WORDS (Continue on reverse side if necessary and identify by block number) Carbon vapor pressure Carbon melt temperature Carbon vaporization coefficients Carbon emissivity Laser-induced phase change Particulate absorption Infrared spectroscopy		
20. ABSTRACT (Continue on reverse side if necessary and identify by block number) This effort has been devoted to gaining a better understanding of the energy-dissipating efficiency of carbon materials. Equilibrium thermochemical properties and kinetic vaporization rate information have been obtained for temperatures approaching 4500°K. A nonequilibrium ablation model and carbon laser vaporization experiments were used to determine the total vapor pressure, melt temperature limits, and the temperature dependence of carbon vaporization (rate) coefficients for different types of graphite. In addition, rough surface emissivities for these graphites were measured, and a preliminary study of the effects of carbon		

UNCLASSIFIED

SECURITY CLASSIFICATION OF THIS PAGE (When Data Entered)

19. KEY WORDS (Continued)

20. ABSTRACT (Continued)

particles on infrared radiation transport in a laser-vaporized carbon plume was carried out. This information makes possible the reliable prediction of the performance of the carbon material thermal protection systems in extreme heat transfer environments. The measured vapor pressures are two to three times higher than those given by the current JANAF tables, and the melt temperature limits are 300 to 600°K higher than current literature values. To our knowledge, our data represent the first reported temperature dependence of carbon vaporization coefficients.

*Original suggested keywords
in situ, Laser-induced plasma chemistry, Particulate
ablation and Infrared spectroscopy.*

SECURITY CLASSIFICATION OF THIS PAGE (When Data Entered)

UNCLASSIFIED

PREFACE

This work was supported by the Office of Naval Research under AF/SD Contract No. F04701-82-C-0083. The first author wishes to especially thank contract monitor Dr. L. H. Peebles, Jr., for the opportunity to carry out this work. Dr. G. M. Rosenblatt contributed greatly to the successful accomplishment of overall program objectives. The laser operating and diagnostics trouble-shooting support of T. A. Park, L. Fishman, and their co-workers in the Aerospace Materials Sciences Laboratory is gratefully acknowledged. Drs. R. Edwards and S. Starrett were very helpful in supplying Graphnol material samples.

Accession For	
NTIS GRA&I	<input checked="checked" type="checkbox"/>
DTIC TAB	<input type="checkbox"/>
Unannounced	<input type="checkbox"/>
Justification	
By	
Distribution/	
Availability Codes	
Avail and/or	
Dist	Special
A1	



CONTENTS

I.	INTRODUCTION.....	1
II.	EMISSIVITY DATA AND ANALYSIS.....	11
	A. Experimental Technique.....	11
	1. Approach.....	11
	2. Apparatus.....	12
	3. Operating Procedure and Data.....	16
	B. Data Analysis.....	17
III.	GRAPHITE VAPORIZATION KINETICS.....	23
	A. Basic Definitions and Importance of Vaporization Coefficients.....	24
	B. Prior Results and Conclusions.....	26
	C. Best Estimate Numerical Values of α for Pyrolytic Graphite and Graphnol.....	30
IV.	PARTICLE EFFECTS.....	33
	A. Particle Effects Spectroscopy.....	33
	B. Experimental Apparatus and Operating Procedure.....	34
	1. Vacuum Chamber.....	34
	2. CO ₂ Laser Transfer Optics.....	40
	3. Diagnostics.....	41
	4. Operating Procedure.....	41
	C. Experimental Results.....	42
	1. First Experiments.....	42
	2. Effect of Varying Graphite Material and Probe Axial Location.....	49
	3. Effect of Finite Ambient Pressures.....	52
	D. Observations.....	55

CONTENTS (Continued)

V. SUMMARY AND CONCLUSIONS.....	61
REFERENCES.....	65
INDEX OF TECHNICAL REPORTS.....	67
INDEX OF PUBLICATIONS.....	67
APPENDICES:	
A. ONE-DIMENSIONAL STEADY-STATE ABLATION OF A SLENDER ROD.....	A-1
B. PARTICLE SIZES DERIVED FROM SETTLING TIMES.....	B-1

FIGURES

1.	Emissivity Experiment Hardware.....	13
2.	Sample and Holder Mounted for Laser Irradiation.....	14
3.	Samples of Several Graphites in Holders.....	15
4.	Graphnol Pyrometer Data.....	18
5.	Poco Pyrometer Data.....	19
6.	Pyrolytic Graphite Parameter Data.....	20
7.	Measured Vaporization Coefficients for Pyrolytic Graphite.....	27
8.	Vaporization Coefficients Comparison for Assumed Emissivities.....	28
9.	Best Estimate Vaporization Coefficients for Pyrolytic Graphite.....	31
10.	Vaporization Coefficients Comparison for Measured Emissivities.....	32
11.	Typical Background Spectra.....	35
12.	Vacuum Chamber, Laser Transfer Optics, and Diagnostics.....	36
13.	Vacuum Chamber and Optical Bench.....	37
14.	Internal View of Vacuum Chamber.....	38
15.	Close-Up View of Graphite Rod Sample Mounted Along Chamber Axis.....	39
16.	Probe Beam Geometry.....	44
17.	4-8 μm Plume Spectroscopy (Run 22-1).....	46
18.	7-12 μm Plume Spectroscopy (Run 23-2).....	48
19.	Laser-on Spectroscopy.....	50
20.	Laser-on Spectroscopy Close to End of Rod.....	51
21.	Probe Beam Transmission Recovery Effects.....	53
22.	Spectra at Various Chamber Pressures.....	54

FIGURES (Continued)

23.	4-8 μm Spectroscopy, Chamber Pressure = 1 atm, $x/d=6$	56
24.	Post-test Appearance of Graphnol Rod (16X).....	57
25.	Axial Distribution of Condensation Factors and Particles.....	59
A-1.	Energy Partitioning at Surface.....	A-2
B-1.	Relationship of Particle Size to Settling Velocity.....	B-2

TABLES

1.	Spectroscopy Runs.....	45
A-1.	Dependence of Calculated Results on Surface Emissivity and Temperature.....	A-7
A-2.	Sensitivity to Rod Diameter.....	A-9
A-3.	Sensitivity to Thermal Conductivity.....	A-9

1. INTRODUCTION

Carbon materials are widely used for thermal protection system applications involving very high temperatures and energy fluxes. The objective of our four-year contract research program has been to gain a better understanding of the superior energy-dissipating efficiency of these materials and, in particular, to determine the limits of their outstanding performance. During the first two years of effort, three uncertain aspects of carbon ablation behavior were studied:

- a. Vapor pressure of carbon
- b. Melt temperature of carbon
- c. Vaporization kinetics of carbon

Carbon laser vaporization experiments and a nonequilibrium ablation analysis were carried out to obtain basic information concerning the above properties. Our first interim report¹ contains a description of the experiments, the analytical approach, and a preliminary analysis. Detailed data analyses and conclusions concerning these carbon thermochemical properties are given in the second interim report,² as well as in Refs. 3 and 4.

¹Baker, R. L., "Carbon Nonequilibrium Phase Change," Office of Naval Research Interim Report, TR-0081(6728-02)-1, The Aerospace Corporation, El Segundo, CA, Dec. 1981.

²Baker, R. L. and M. A. Covington, "The High Temperature Thermochemical Properties of Carbon," Office of Naval Research Interim Report, TR-0082(2729)-1, The Aerospace Corporation, El Segundo, CA, Mar. 1982.

³Baker, R. L., M. A. Covington, and C. M. Rosenblatt, "The Determination of Carbon Thermochemical Properties by Laser Vaporization," High Temperature Materials Chemistry Symposium, The Electrochemical Society (1983) pp. 143-154.

⁴Baker, R. L., M. A. Covington, and G. M. Rosenblatt, "The Vapor Pressure, Melt Temperature and Vaporization Kinetics of Carbon," J. Appl. Phys., (To be published.)



During our third year of effort, laser ablation experiments and analyses were carried out and reported for metal-impregnated carbon materials. In addition, higher order numerical simulations of a nonequilibrium ablation process were performed and reported.^{5,6} This latter work confirmed the approximate analysis methods we had previously used for obtaining carbon thermochemical properties from our laser ablation data.

This final report describes additional experiments and analyses carried out during the past year. Our present objectives are closely related to prior work. They include determination of both the relative surface emissivities and the vaporization kinetics of different types of graphite. Emissivity and vaporization kinetics effects are discussed in Sections II and III, respectively.

An additional objective of recent work has been to investigate other effects. It is of particular interest and importance to determine the character and extent of carbon particulates in the expanding carbon vapor and their effect on the transport of infrared wavelength radiation through the plume. A new test chamber and infrared spectroscopic instrumentation were fabricated this past year to study these effects. The test apparatus, instrumentation, and initial experimental results are discussed in Section IV.

An overall summary and conclusions from our four-year effort are given in Section V.

⁵Turner, J. S., "Laser-Induced Phase Changes at Solid Surfaces," Final Report, The University of Texas at Austin, October 1982.

⁶Baker, R. L., D.A. Nelson, and J. S. Turner, "Higher Order Numerical Simulations of the Knudsen Layer," Office of Naval Research Interim Report, TR-0083(3729)-2, The Aerospace Corporation, El Segundo, CA, Mar. 1983.

II. EMISSIVITY DATA AND ANALYSIS

Our interest in determining the high temperature emissivities of different graphites stems from the vaporization kinetics studies we have carried out. As shown in Refs. 2-4, and further discussed in Section III, the experimentally measured relative vaporization kinetics, for different graphites, are very sensitive to the values of the surface emissivity used to determine the surface temperatures. Because of this and a lack of high temperature emissivity data for ablation-roughened samples in the literature, new experiments were specifically designed and carried out to determine this information. The experiments, data, and analysis are discussed below.

A. EXPERIMENTAL TECHNIQUE

1. Approach

Due to difficulties associated with making measurements at temperatures above 2000°K and the small ablated (roughened) sample areas available, it was necessary to design an experimental technique specifically for our purposes. Dr. G.M. Rosenblatt* suggested that small samples of the graphite for which the emissivity is desired could be embedded in the surface of a bulk sample of a graphite for which the emissivity is known. Then, by bringing the bulk graphite, with its embedded sample, up to a high temperature and measuring the irradiance from its surface and from the sample surface, the emissivity of the sample could be determined from the relative irradiance values. If it is assumed that the temperatures of the two materials are the same, then the relative irradiance is a direct measure of the relative emissivities.

* Personal communication, Los Alamos National Laboratory, Los Alamos, N. M.

2. Apparatus

As originally envisioned, the bulk graphite was to be resistively heated. For the experiments that were carried out, the graphites were laser-heated. The "bulk" graphite sample-holder consisted of a pyrolytic graphite cylinder 8.5 mm in diameter and 4 mm long with a 3-mm diameter sample hole on its axis. A photograph of two sample-holders is shown in Fig. 1a. A second hole, shown in the cylindrical surface of the holder on the right, accommodated a post used to hold the sample-holder and sample in place. A photograph of the entire assembly, including sample-holder, sample, and post, positioned inside a 5-mm thick graphite radiation shield is shown in Fig. 1b.

In order to irradiate one face of the sample and holder with a laser and measure the relative irradiance on the opposite face, the radiation shield with the sample assembly inside was attached to a 1/2-in. thick graphite plate and positioned onto the centerline of the vacuum chamber apparatus described in Section V. This setup is shown schematically in Fig. 2. The laser beam was defocussed in order to uniformly flood-load the face of the sample and holder. Using a quartz viewing window located in a port on the rear of the chamber, we found it possible to directly view the opposite face with a scannable pyrometer.

A close-up photograph of a sample and holder in the radiation shield is shown in Fig. 3a. The pyrolytic graphite holders were fabricated so that the planes of this highly anisotropic material were perpendicular to the axis of the support post. This accomplished several important objectives:

- It minimized heat transfer losses into the supporting post, which was also made from pyrolytic graphite with the planes perpendicular to the post axis. (The thermal conductivity perpendicular to the planes is 200 times less than in the directions parallel to the planes.)⁷

⁷Touloukian, Y. S., ed., Thermophysical Properties of Matter, Vol. 8, IFI/Plenum Press, NY, 1970.

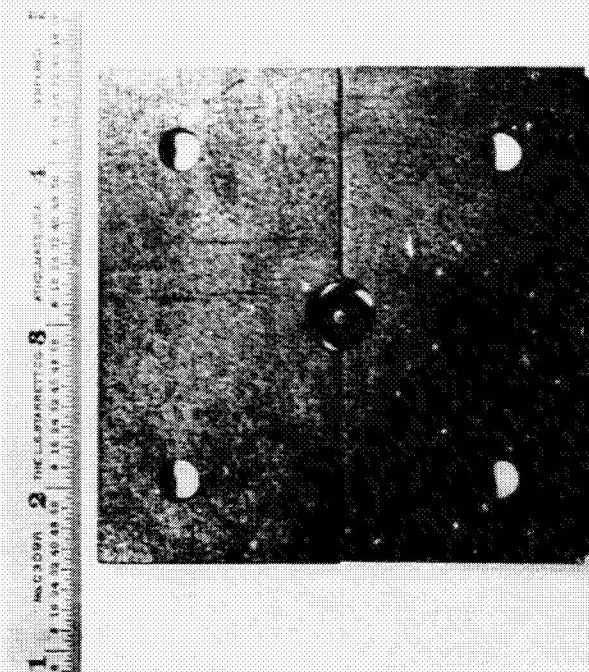
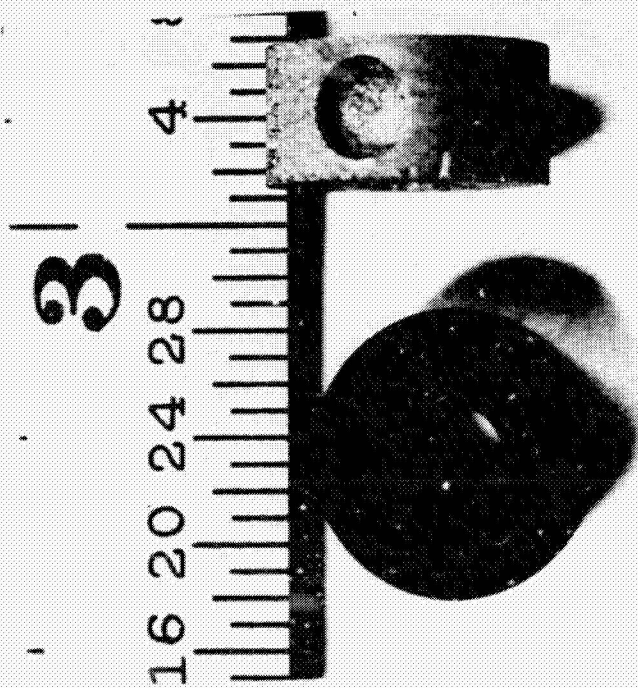


Fig. 1. Emissivity Experiment Hardware

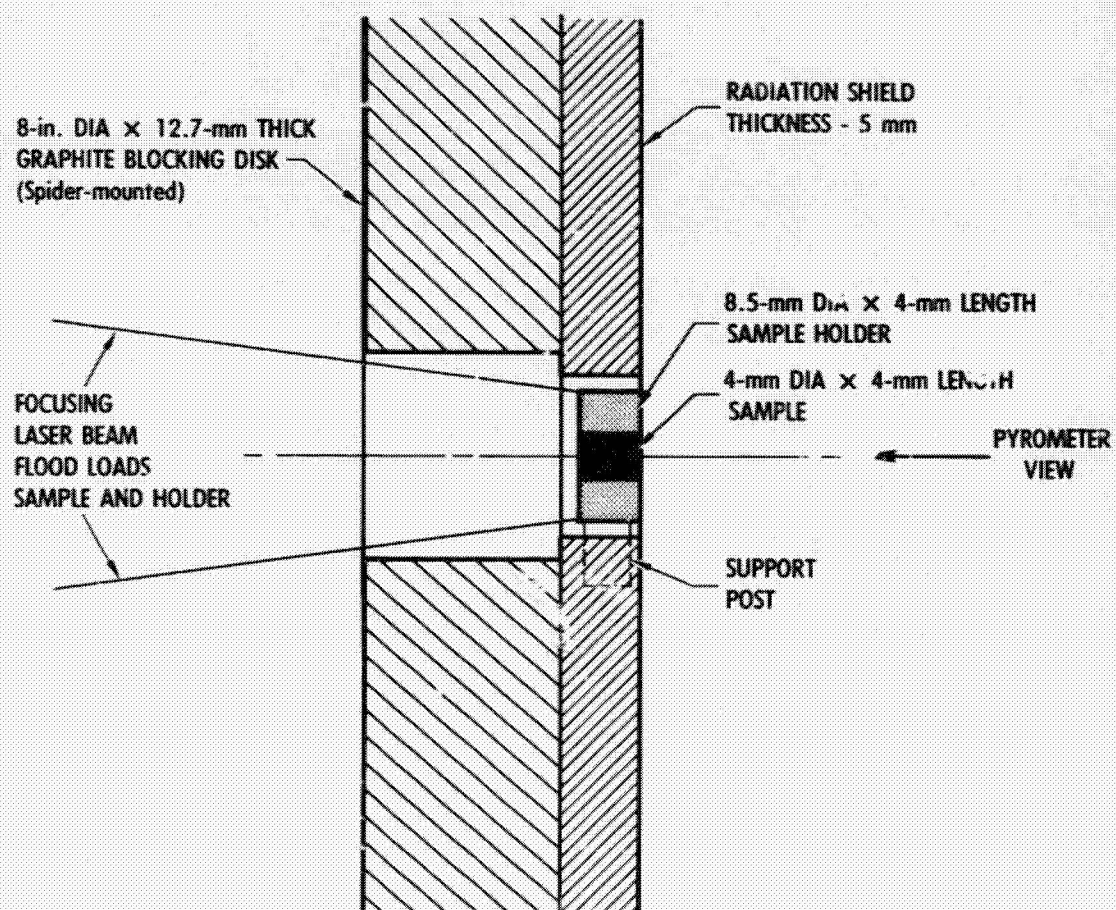


Fig. 2. Sample and Holder Mounted for Laser Irradiation

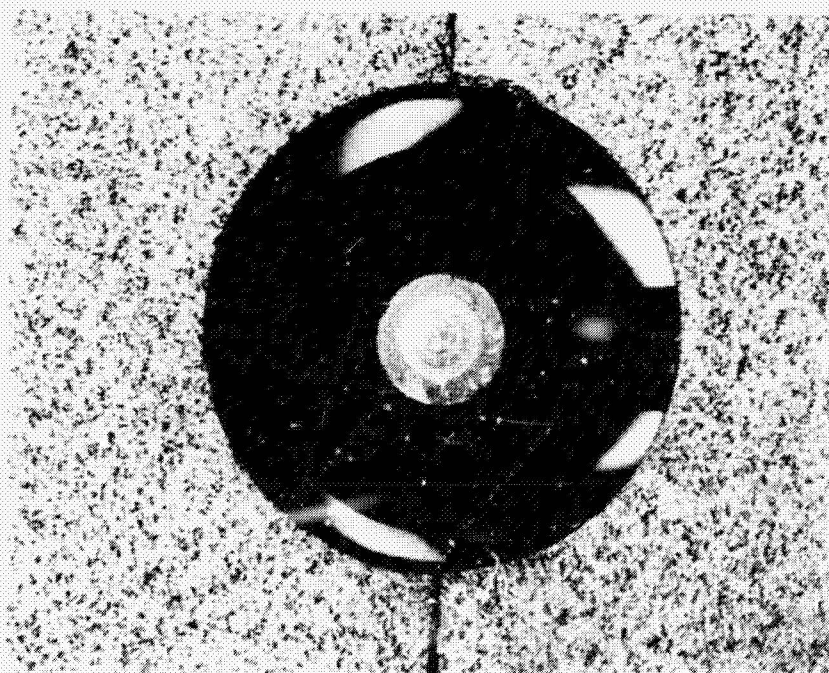


Fig. 3. Samples of Several Graphites in Holders

- It insured a very high thermal conductivity from the front (laser irradiated) to the back of the sample-holder, thus minimizing temperature gradients and maximizing laser energy transport into the sample-holder.
- It exposed the edges of pyrolytic graphite planes to both the incoming laser irradiation as well as the viewing pyrometer. Since the literature^{7,8} supports a unit emissivity value for pyrolytic graphite looking edge-on to the planes, the absorbed laser energy was maximized and the relative emissivity of the sample in the center could be compared with the unit emissivity of the sample-holder.

The surfaces of the 3-mm diameter x 4-mm long cylindrical samples, to be viewed by the pyrometer, were pre-roughened by focussing the laser on them for 1-2 sec in an atmospheric air environment. A photograph of roughened samples of the three graphites for which emissivity measurements were made is shown in Fig. 3b.

3. Operating Procedure and Data

The 1 kW CO₂ laser used to heat the sample-holder with a sample inserted is described in Section V. Normal operating procedure called for irradiation at nominal on-sample laser power levels of 500, 700, and 900 W. At each power level, sufficient time (15-30 sec) was allowed for steady-state temperatures to be reached. The pyrometer was then mechanically scanned horizontally across the entire sample-holder along a line passing through the centerline (axis) of the sample. The pyrometer (Thermogage Model 8000-10)⁹ had a nominal spot size of 1/16 in. (1.59 mm) and a focal length of 30 in. (76 mm). Remotely operated and electrically driven micrometers were used to

⁸Pyrolytic Graphite Handbook, Metallurgical Production Department, General Electric Company, Schenectady, NY, 1964, as quoted in Gokcen, N.A., et. al., "Determination of Graphite/Liquid/Vapor Triple Point by Laser Heating," High Temperature Science, Vol. 8, June 1976, pp 81-97

⁹Brookley, C.E., "Product Data for High Temperature Pyrometers," Thermogage, Inc., Frostburg, MD, 1982. Also, "Calibration Curves for the Aerospace High Temperature Pyrometer."

sweep the pyrometer spot from one edge to the other edge of the sample-holder in about 30 sec. After two or more scans at a given laser power level, the power was increased and the procedure repeated.

Experimental data obtained in this manner for graphite samples consisting of Graphnol N3M¹⁰, Poco (AXF.Q1), and pyrolytic graphite (Super Temp, continuously nucleated) are shown in Figs. 4, 5, and 6, respectively. In each figure, the relative sizes of the sample-holder, sample, and pyrometer spot are shown at the top; the pyrometer signals obtained by scanning at each of three laser power levels are seen in the lower half of the figure.

B. DATA ANALYSIS

When converted to temperatures,⁹ the pyrometer output signals (mV), shown in Figs. 4, 5, and 6, give values ranging from 1780°K to 2120°K for a surface emissivity of 1.00. For emissivity ϵ less than 1.00, the temperature is obtained from the requirement that the surface irradiance is a constant; i.e., $\epsilon T^4 = \text{constant}$, for a given data point.

The pyrometer data shown in Figs. 4 and 5, for the polycrystalline graphites Graphnol and Poco, respectively, indicate a relatively flat output voltage profile across the samples. As the laser power is increased, higher voltages (temperatures) are obtained; but the profiles across the samples remain reasonably flat. Based on our assumption in designing the experiment, that the temperature of the sample is the same as that of the sample-holder, we conclude from these figures that the roughened surface emissivities of Graphnol and Poco graphites are nearly the same as the unit emissivity of the flat surface of the pyrolytic graphite sample-holder.

¹⁰Johnsen, B. P. and H. S. Starrett, "Preliminary Design Data Package for Graphnol N3M (Phase III, Mantech)," Report SORI-MER-82-20, Southern Research Institute, Birmingham, AL, Nov. 1982.

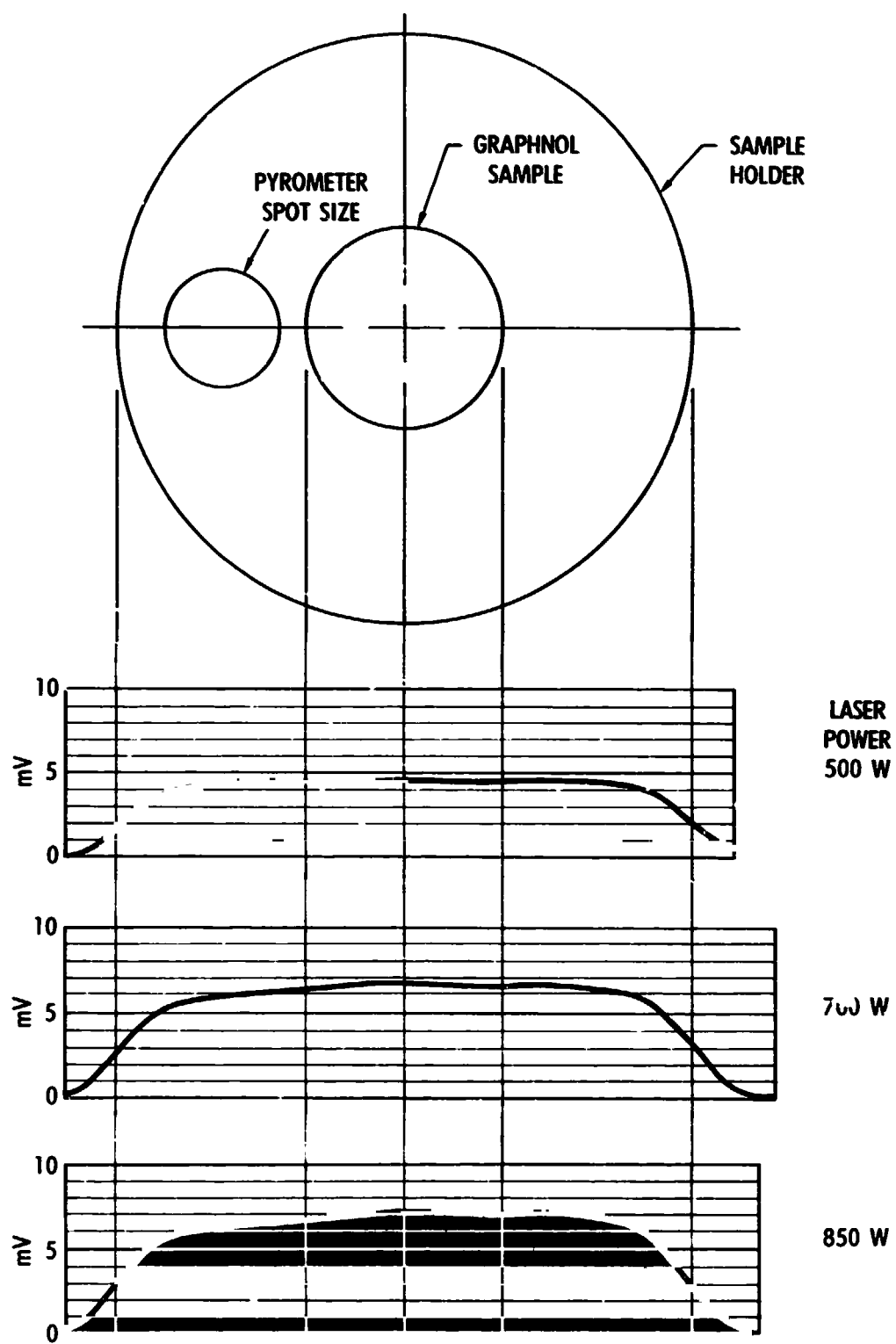


Fig. 4. Graphnol Pyrometer Data

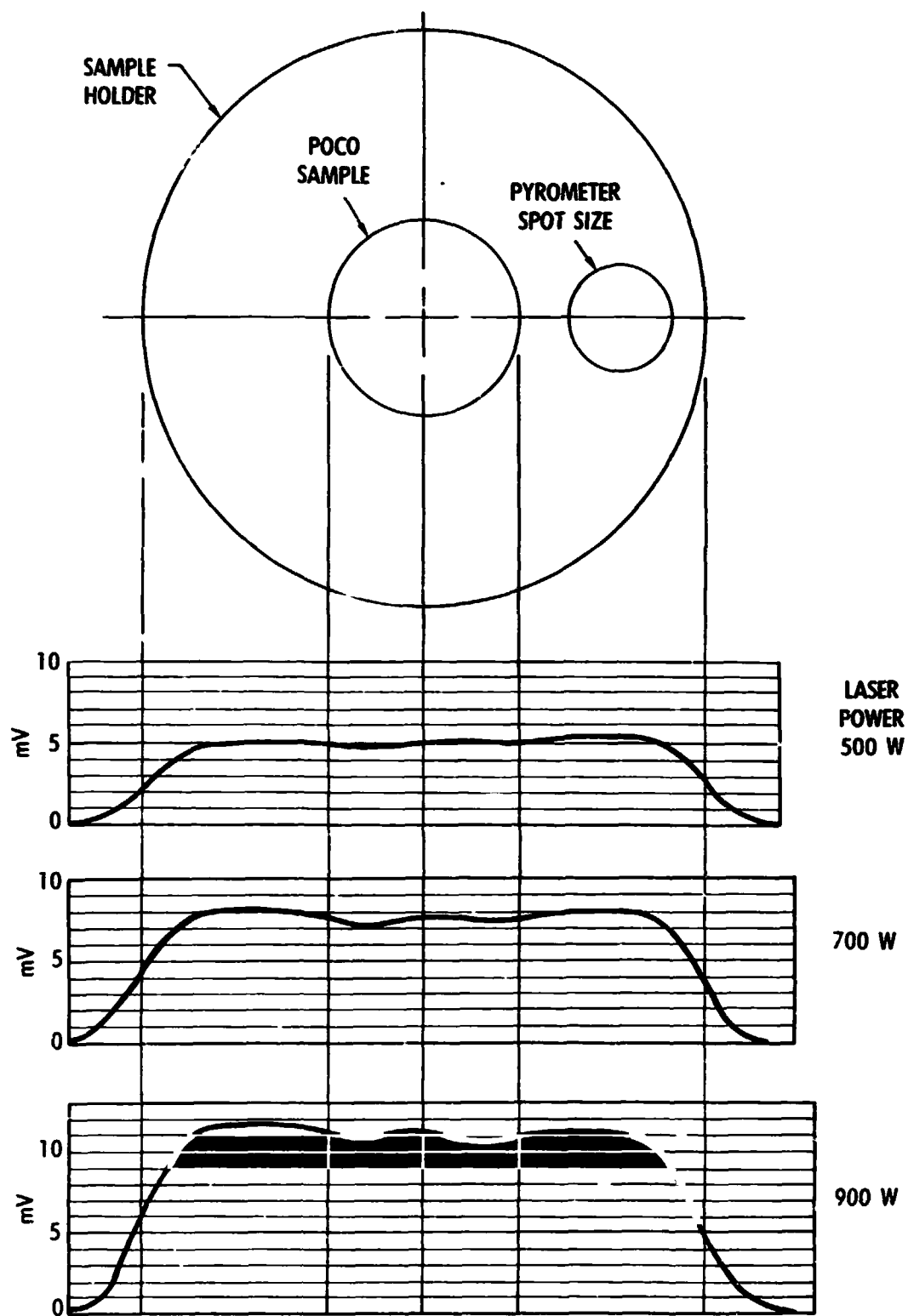


Fig. 5. Poco Pyrometer Data

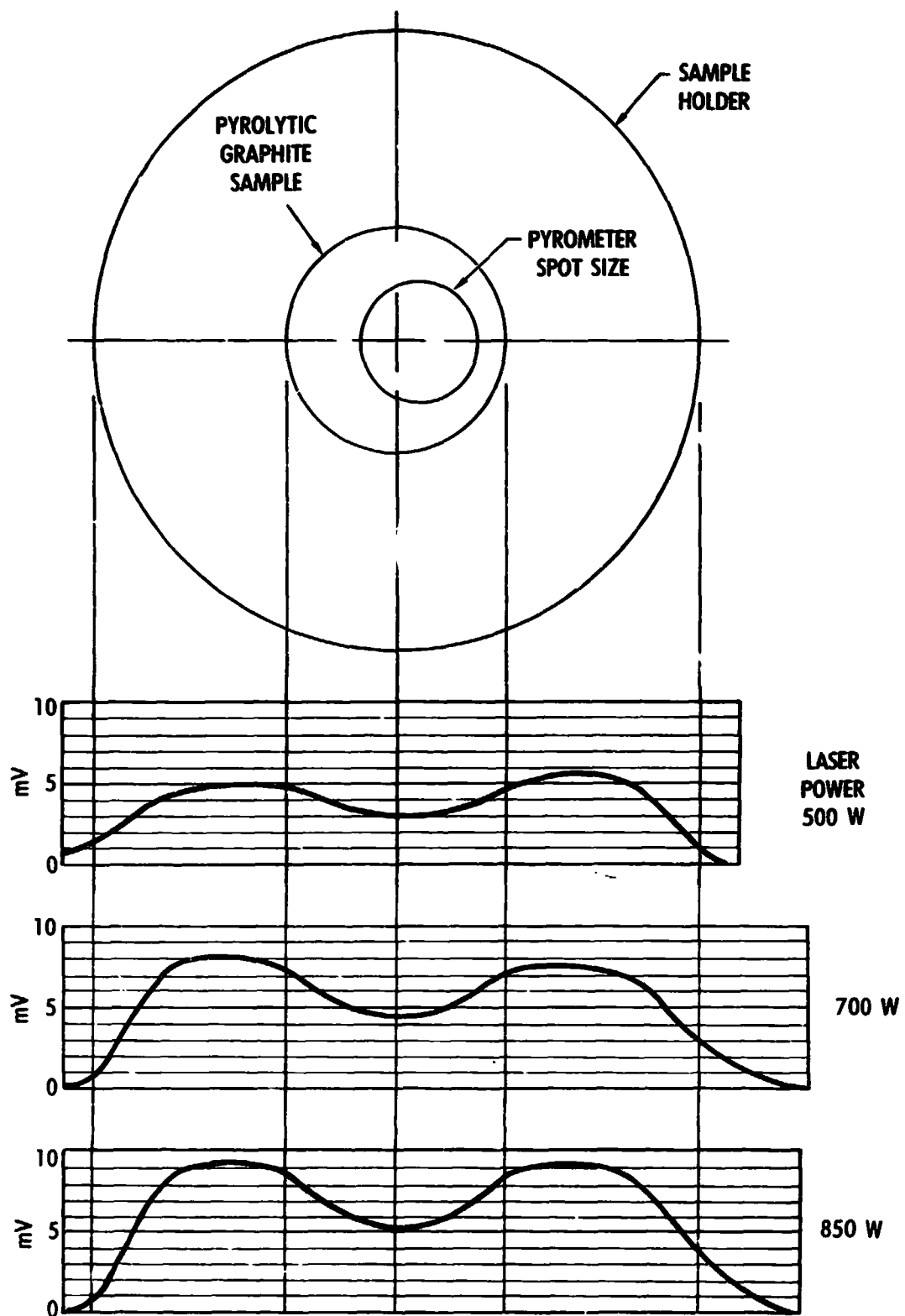


Fig. 6. Pyrolytic Graphite Pyrometer Data

In contrast to the above, the data shown in Fig. 6 for the pyrolytic graphite sample indicate substantially less output signal from the pyrometer when it is scanning the sample. If the sample emissivity is 1.00, then these data indicate sample temperatures 110 to 120°K lower than the temperatures of the sample-holder. However, a more likely explanation is that the sample and sample-holder temperatures are nearly the same, for a given laser power input level, and the lower pyrometer output signal is due to a reduced emissivity of the sample relative to the sample-holder. Interpreted in this way, the data in Fig. 6 indicate a surface emissivity of 0.80 for the pyrolytic graphite sample viewed perpendicular to the lamellar planes. This should be regarded as a lower limit for the emissivity of this material in this direction as discussed below.

As previously mentioned, pyrolytic graphite has a thermal conductivity parallel to the lamellar planes which is 200 times greater than that perpendicular to the planes. For the Fig. 6 data discussed above, laser energy was conducted through the pyrolytic graphite sample-holder along the planes. In contrast, conduction through the pyrolytic graphite sample was perpendicular to the planes. This leads to obvious questions concerning our assumption that the sample and sample-holder, as viewed by the pyrometer (see Fig. 2), are at the same temperature.

Less than one millimeter below the surface where the laser energy enters, the sample temperature is the same as that of the surrounding sample-holder. This conclusion is based upon a highly simplified two-dimensional model of the energy transport and temperature distributions through this sample and sample-holder. From this point until the back surface is approached, very little energy is transported through the sample along its axis because of the extremely low thermal conductivity in this direction. At each axial location beyond this point, the sample temperature is the same as that of the surrounding sample-holder due to very high sample thermal conductivity in the radial direction. As the pyrometer-viewed (back) surface is approached, the sample temperature drops rapidly in order to conduct energy to the surface to be radiated away. The approximate energy balance equations in this region indicate that the temperature seen by the pyrometer on the sample centerline could be 30°K less than the temperature seen on the sample-holder.

If this estimate is reasonable, the drop in pyrometer output signal (seen in Fig. 6 when the sample is viewed) is due to a decreased emissivity of the sample relative to the holder and to a sample temperature slightly less than that of the sample-holder. In this case, rather than the lower bound emissivity of 0.80 previously found, this interpretation of the data indicates an emissivity of approximately 0.85.

An alternate method of determining the high temperature emissivity of pyrolytic graphite has also been developed. Unfortunately, within the constraints of our laser operating time, we were not able to obtain additional data to test this new method. The technique and approach are discussed in Appendix A.

III. GRAPHITE VAPORIZATION KINETICS

An important major conclusion of our earlier work²⁻⁴ was that the vapor pressure of carbon is "best represented" by thermodynamic property data other than that given in the JANAF Tables.¹¹ The recommended data are those of Lee and Sanborn¹² and Leider, Krikorian, and Young.¹³ Since these workers were at the Lawrence Livermore National Laboratory when their results were published, we have referred to these data as the Livermore property data. When these data are used, the predicted carbon total pressures are two to four times greater than those obtained using the JANAF property data.

As discussed below, the rate of mass loss from a solid carbon (graphite) surface is proportional to both the vapor pressure and the vaporization coefficient α . Whereas the vapor pressure is an equilibrium property of the material, the vaporization coefficient is a nonequilibrium (kinetic) parameter which expresses the relative rate of (in this case) the carbon solid-vapor sublimation process. Thus, the importance of obtaining carbon vaporization coefficient conclusions consistent with our Livermore thermodynamic property data conclusion becomes apparent.

Preliminary conclusions regarding numerical values of carbon vaporization coefficients were given in Refs. 2-4. Insofar as we know, these are the only publications in the literature that give an experimentally determined temperature dependence of these coefficients. Subsection A, below, reviews basic definitions and the importance of vaporization coefficients. In

¹¹JANAF Thermochemical Tables, National Bureau of Standards, NBS-37, June 1971.

¹²Lee, E. L. and R. H. Sanborn, "Extended and Improved Thermal Functions for the Gaseous Carbon Species C₁-C₇ from 298 to 10,000°K," High Temperature Science, Vol. 5, 1973, pp. 438-453.

¹³Leider, H. R., O. H. Krikorian, and D. A. Young, "Thermodynamic Properties of Carbon Up to the Critical Point," Carbon, Vol. 11, 1973, pp. 555-563.

Subsection B, our prior results and conclusions concerning carbon vaporization coefficients are presented. Finally, in Subsection C, best estimate numerical values of α are given for pyrolytic graphite and the polycrystalline graphite, Graphnol.

A. BASIC DEFINITIONS AND IMPORTANCE OF VAPORIZATION COEFFICIENTS

Physically, the vaporization coefficient α for a given material represents the relative vaporization rate of that material at a given temperature. It is defined in terms of the maximum possible vaporization rate, i.e.

$$\dot{m}_{\max} = \sqrt{\frac{M}{2\pi RT_s}} p_s,$$

where \dot{m}_{\max} = maximum mass vaporization rate on a unit area/
unit time

M = molecular weight

p_s, T_s = saturated vapor pressure and temperature

R = universal gas constant

The vaporization coefficient defines the relative rate of vaporization; thus

$$\alpha = \dot{m}/\dot{m}_{\max} \text{ and } \dot{m} = \alpha \sqrt{\frac{M}{2\pi RT_s}} p_s,$$

where \dot{m} is the actual vaporization rate at temperature T_s . The Langmuir vapor pressure p_L is defined as the product of α and p_s ¹⁴

$$p_L = \alpha p_s = \dot{m} \sqrt{\frac{2\pi RT_s}{M}}$$

¹⁴Rosenblatt, G. M., "The Role of Defects in Vaporization: Arsenic and Antimony," Surface Defect Properties of Solids, Vol. 5, 1976, pp.36-64.

If the Langmuir vapor pressure can be determined experimentally as a function of T_s , then by knowing $p_s(T_s)$ one can determine the temperature dependence of α from the data.^{2,4}

The discussion above assumes that the vaporization process takes place into a vacuum with no vaporized atoms or molecules backscattered to the vaporizing surface. In Refs. 2 through 4, an analysis method based upon a model of a nonequilibrium vaporization process was developed which allows the Langmuir vapor pressure p_L to be determined from experimental data taken in non-vacuum, i.e., finite back-pressure, environments. Once the temperature dependence of p_L has been measured, α as a function of T_s can be determined in the same manner as discussed above. This is illustrated in Subsections B and C below.

Why is a knowledge of vaporization coefficient values important? The primary reason is that for materials such as carbon (graphite), which vaporize subject to kinetic constraints, the rate of mass loss (ablation) for a given energy input to the surface cannot be predicted unless both the vapor pressure p_s and the vaporization coefficient α are known.

Another reason we need to determine the vaporization coefficients of different graphite materials is to compare their vaporization kinetics to their solid state structure (crystallinity) and to each other. Generally speaking, for a given rate of energy input to a graphite surface, the material with the lowest vaporization coefficient will achieve the highest surface temperature. This is because the low vaporization coefficient value implies slow kinetic rates; to increase the vaporization rate to that required for maintaining an energy balance, a higher temperature is needed. Following through on this idea, a graphite material with vaporization coefficients less than those of other graphite materials can be melted, i.e., it reaches the melt temperature, at energy flux levels lower than those required for the material with higher vaporization coefficients. Because melting degrades the ablation efficiency, differences such as these are important to understand and quantify.

B. PRIOR RESULTS AND CONCLUSIONS

The carbon laser ablation experiments which were carried out specifically to evaluate vaporization coefficients for different types of graphite are described in Ref. 1. Both continuous wave (CW) as well as pulsed laser experiments were performed. The mathematical model developed to describe the carbon nonequilibrium ablation process is described in Refs. 1 and 2. Data analysis, using the model to obtain numerical values of vaporization coefficients from the measured data, is contained in Refs. 2-4. Our vaporization coefficient conclusions from these analyses are summarized in Figs. 7 and 8.

Figure 7 illustrates our results for pyrolytic graphite. The lower solid line shows the measured temperature dependence of the vaporization coefficient as obtained from the CW laser data. For these data, both the laser illumination/ vaporization and the pyrometer viewing took place in a direction parallel to the pyrolytic graphite planes. In this direction, an assumed surface emissivity ϵ of unity is supported by the literature.⁸ This alleviates uncertainties associated with measured surface temperatures and lends confidence to the vaporization coefficient values shown in Fig. 7 for the temperature range from 3300 to 4000°K.

The upper solid line, obtained from pulsed laser data, has a slightly higher slope and extends measured vaporization coefficient values from 4000°K up to 4500°K. We note three observations concerning this line. First of all, the line is for an arbitrarily assumed surface emissivity of 0.97. Second, the extrapolated numerical value of α approaches unity at the Livermore triple-point (melt) temperature of 4765°K. Finally, at 4000°K both solid lines indicate approximately the same values of α .

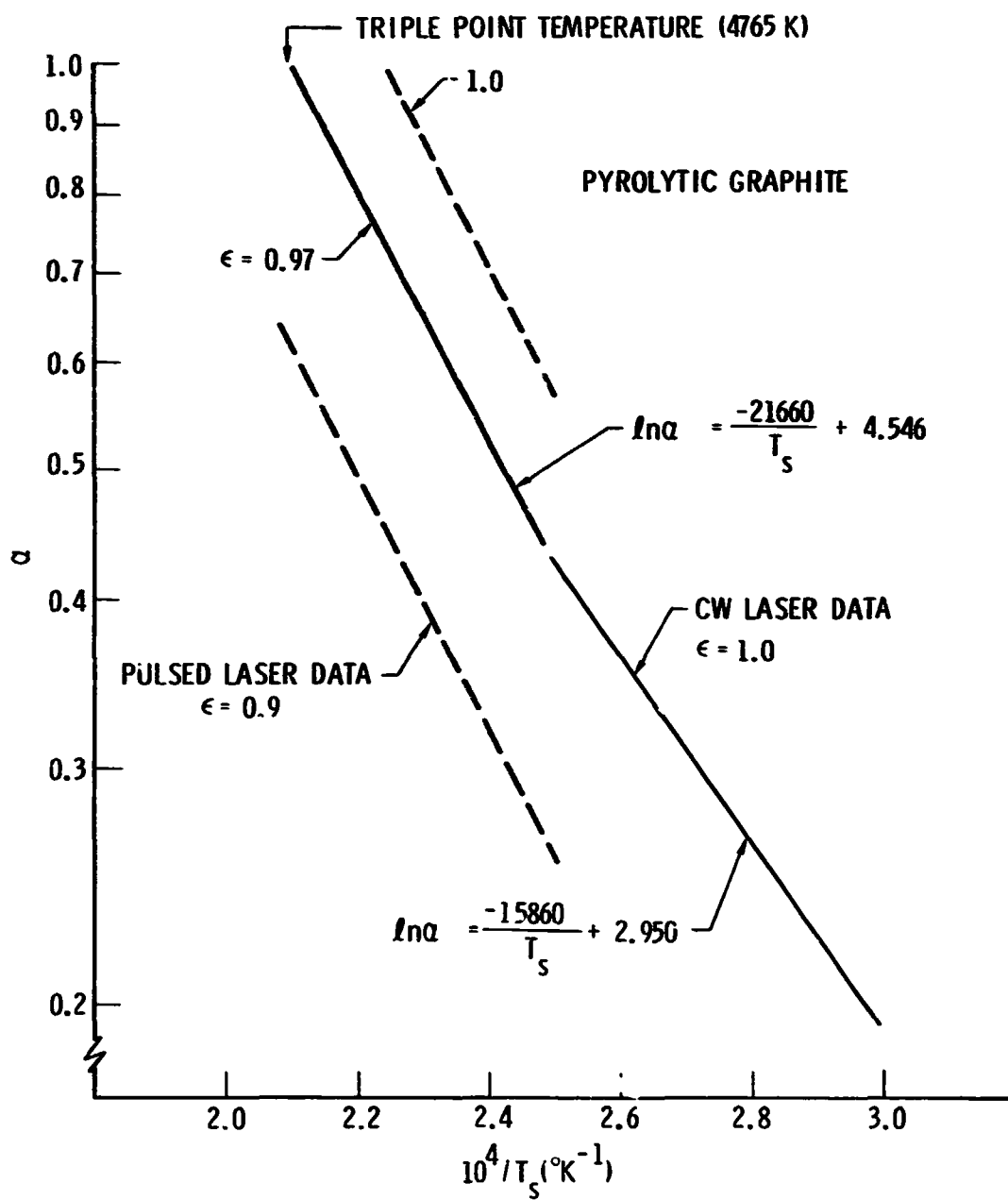


Fig. 7. Measured Vaporization Coefficients
for Pyrolytic Graphite

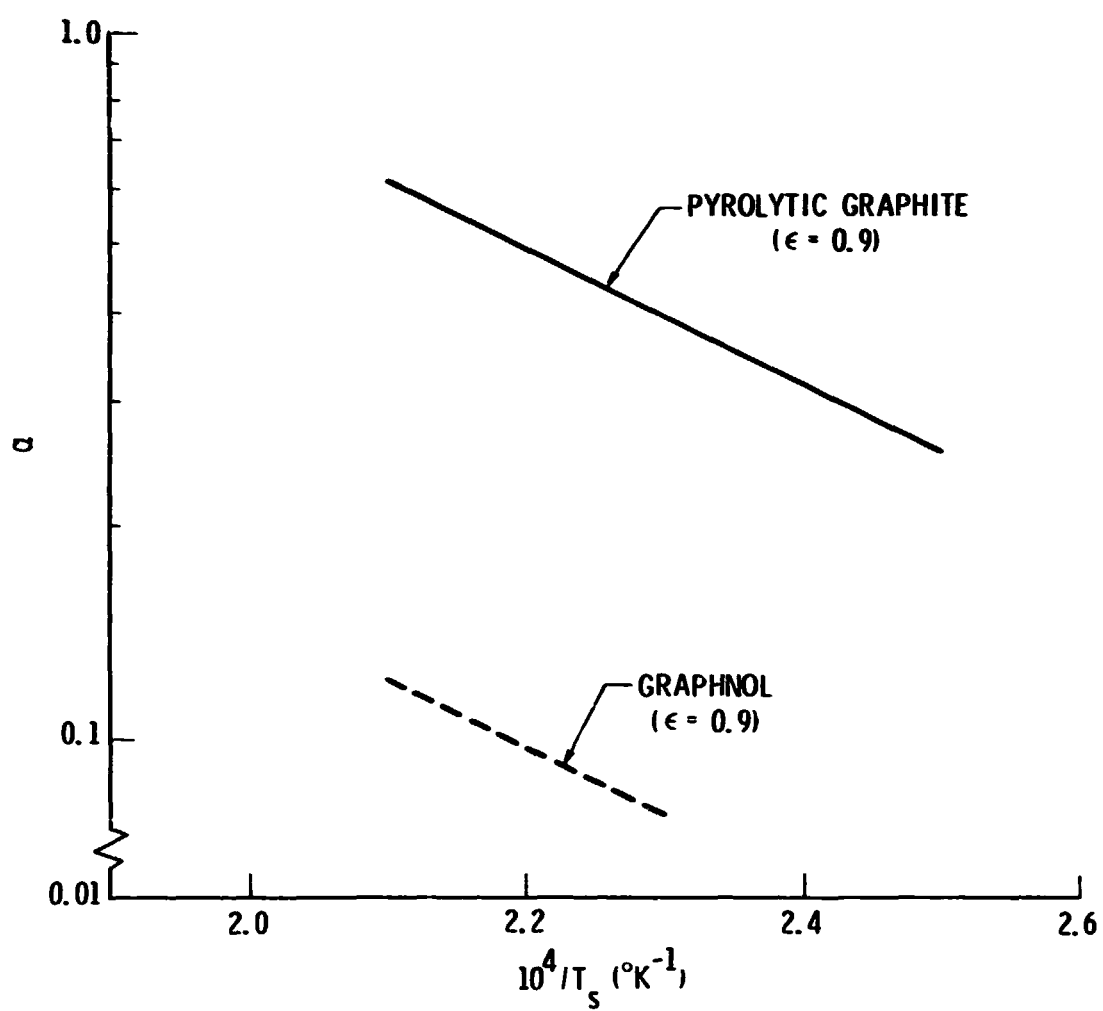


Fig. 8. Vaporization Coefficients Comparison for Assumed Emissivities

The laser illumination/vaporization and pyrometer viewing for the pulsed laser data (upper solid line) were in a direction perpendicular to the pyrolytic graphite planes. In this direction, there is much greater uncertainty regarding the values of the surface emissivity ϵ . The sensitivity of the data interpretation to the value assumed for the surface emissivity is illustrated by the two dashed lines in Fig. 7 which are for ϵ values of 0.9 and 1.0. Thus, the importance of determining the correct value of ϵ is noted (see Section II).

Additional experimental data were obtained in both the CW and the pulsed laser experiments to evaluate vaporization coefficients for the polycrystalline graphite, Graphnol. Unfortunately, the CW laser data were ultimately determined to be uninterpretable because of complications related to the necessary presence of oxygen in the chamber.² However, numerically determined vaporization coefficients for both pyrolytic graphite (perpendicular to the planes) and Graphnol, obtained from the pulsed laser data, are shown in Fig. 8. It was assumed that both materials had a surface emissivity of 0.9. For this assumption, measured values of α for Graphnol are a factor of 5 lower than for pyrolytic graphite at a given temperature. The overriding importance of knowing the surface emissivity values is again apparent. In this case, little can be said about the relative vaporization kinetics of the two graphites until their associated surface emissivities are known.

In Section II, numerical values of high temperature surface emissivity were determined from our recent experimental data for ablation-roughened samples of Graphnol and pyrolytic graphite (perpendicular to the planes). In Subsection III-C below, these values are used to reinterpret our original pulsed laser data. This eliminates the arbitrary emissivity value assumptions associated with the above discussion of Figs. 7 and 8 and allows "best estimate" values of α to be determined for these materials.

C. BEST ESTIMATE NUMERICAL VALUES OF α FOR PYROLYTIC GRAPHITE AND GRAPHNOL

In the following discussion, vaporization coefficients and emissivities are designated $\alpha_{||}$, $\epsilon_{||}$, and α_{\perp} , ϵ_{\perp} for pyrolytic graphite parallel and perpendicular to the planes, respectively. When the emissivity value (ϵ_{\perp}) of 0.85 (determined for pyrolytic graphite in Section II) is used, the vaporization coefficient values (α_{\perp}) interpreted from our pulsed laser data are shown by the solid line on the left in Fig. 9. Also shown by the line on the right are the values of $\alpha_{||}$ obtained from our CW laser data. We note that at 4000°K, the pyrolytic graphite vaporization coefficient α_{\perp} for vaporization taking place perpendicular to the planes is about a factor of three lower than $\alpha_{||}$ for vaporization occurring parallel to the planes. A plausible explanation of this behavior is that for vaporization that occurs parallel to the planes, i.e., from an a-b face, etch pits formed in the vaporizing surface create more "kinks" or active sites¹⁶ than when the vaporization takes place perpendicular to the planes, i.e., from a c-face. The greater number of kink sites in the former case leads to more rapid vaporization rates within the context of the classical "terrace-ledge-kink" model of solid vaporization processes.¹⁴⁻¹⁶

A comparison of high temperature vaporization coefficients for pyrolytic graphite and Graphnol is shown in Fig. 10. Again, the values shown were obtained from our pulsed laser data using the values of surface emissivity determined for these materials in Section II. Recall that the same data were interpreted assuming that both materials had an emissivity of 0.9 in Fig. 8. Figure 10 indicates that within the limits of our ability to determine emissivities, mass loss rates, and temperature, these two materials differ very little in their kinetic rates of vaporization.

¹⁵Rosenblatt, G. M., "Evaporation from Solids," Treatise on Solid State Chemistry, Vol. 6a, N.B. Hannay, ed., Plenum Press, N.Y., 1976, p. 199.

¹⁶Hirth, J. P. and G. M. Pound, "Condensation and Evaporation," Progress in Materials Science, Vol. 11, MacMillan, New York, 1963.

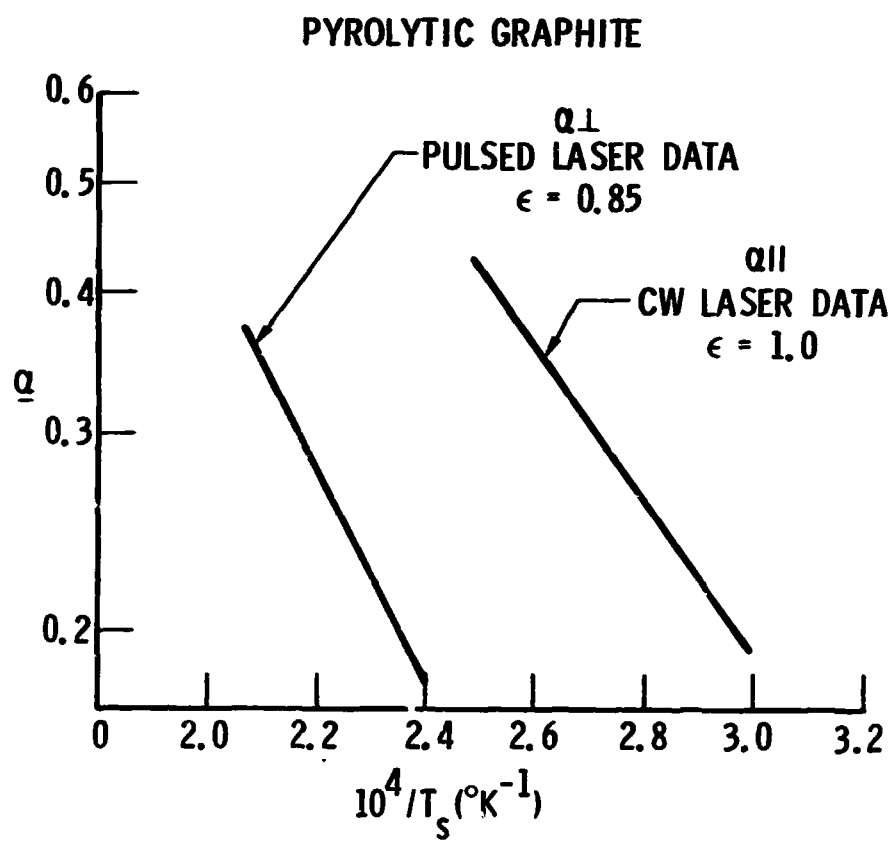


Fig. 9. Best Estimate Vaporization Coefficients for Pyrolytic Graphite

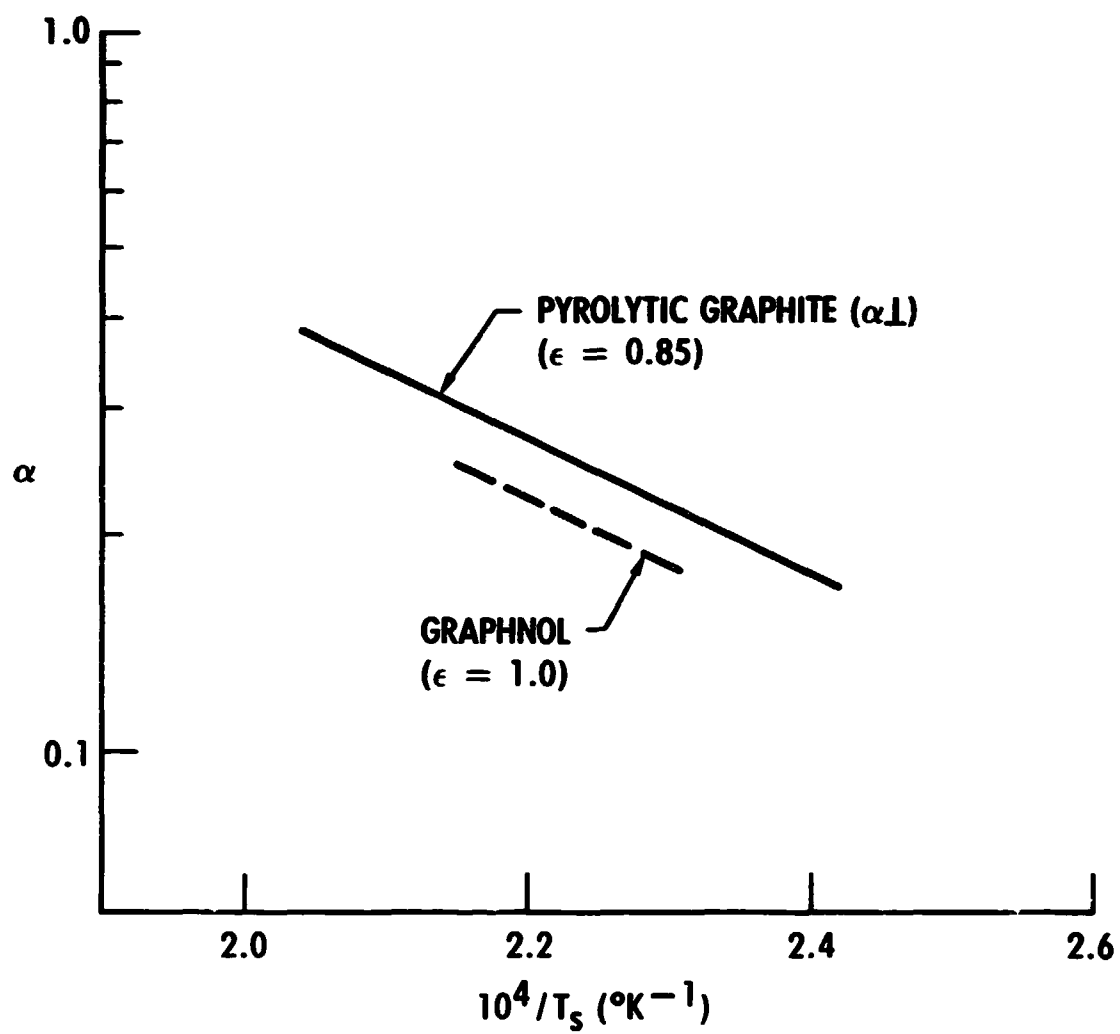


Fig. 10. Vaporization Coefficients Comparison for Measured Emissivities

IV. PARTICLE EFFECTS

Our earlier experiments¹ dramatically showed the significant carbon particulate condensation, and consequent laser-beam blockage effects, which can occur when carbon is laser-vaporized into an inert gas (argon) atmosphere. The purpose of the work described herein was to begin to quantify these effects for ambient conditions, ranging from atmospheric pressure to near-vacuum conditions, by using infrared spectroscopic methods to probe the carbon vapor-particle plume flowfield. In Subsection A below, a brief overview is given of the spectroscopic methods we have used. A more detailed description of the experimental apparatus, spectroscopic methods, and basic operating procedure is given in Subsection B. Initial experimental results and observations are then discussed in Subsections C and D, respectively.

A. PARTICLE EFFECTS SPECTROSCOPY

Infrared spectroscopy at various positions in a CO₂ laser-generated carbon plume is capable of providing the following plume diagnostic information:

- o Spectral transmission profiles
- o Temporal variations in transmission
- o Measurement of particulate growth rate
- o Estimates of average particulate size
- o Observation of molecular constituents (e.g., C₃)
- o Laser blockage effects
- o Plume-scattering properties at 10.6 μ m
- o Particulate heating/cooling rates
- o Condensation rates in vacuum plumes
- o Inert gas effects on condensation rates

Because of the large number of unknowns, our initial efforts can be described as survey experiments. Low resolution infrared spectroscopy, using circular variable interference filters (CVIF), was selected as the optimum method of performing the initial diagnostics. CVIFs are easy to use, are capable of reasonably fast spectral scan time, and have high optical

through-put. For our setup, this meant 1 to 2 percent spectral resolution and a 0.75-sec scan time.

Available CVIFs were used, which restricted our measurements to a 4-8 μm scan or a 7-12 μm scan. A typical background spectrum is shown in Fig. 11. Note that under the conditions described above and using a sensitive Hg:Cd:Te detector, cooled to 77°K, a signal to noise of approximately 20/1 was available for these studies. This provided useful spectroscopy as evidenced by the appearance of the strong 6 μm H_2O absorption from the external 1.2 m optical path. Certainly, good plume transmission data could be gathered over large portions of the 4-12 μm spectral region. This range also encompasses the interesting 5.2 μm rotation-vibration band for the C_3 molecule.¹⁷

B. EXPERIMENTAL APPARATUS AND OPERATING PROCEDURE

Our experiments were conducted in the 2-ft diameter vacuum facility shown schematically in Fig. 12 and pictorially in Figs. 13, 14, and 15. The major facility subsystems comprise the vacuum chamber, CO_2 laser transfer optics, and the diagnostics.

1. Vacuum Chamber

A stainless-steel vacuum chamber was available and measured 2 ft in diameter by 2.5 ft in length. The chamber was modified to focus the CO_2 laser energy on the end of a 3-mm diameter x 25-mm length carbon rod. The rods can be positioned at various distances from the front of the chamber. Optical ports were cut in the sides of the chamber to permit infrared spectral probing through KCl windows across the effluent carbon plume. The ability to reposition the carbon rod allowed the spectral probe diagnostics to remain stationary, while particle effects were observed at various distances from the laser-heated carbon source.

¹⁷Treffers, R. R. and D. P. Gilra, "The Vibrational Spectrum of C_3 in the 5 Micron Region," Astrophysical J., Vol. 202, 1975, pp. 839-843.

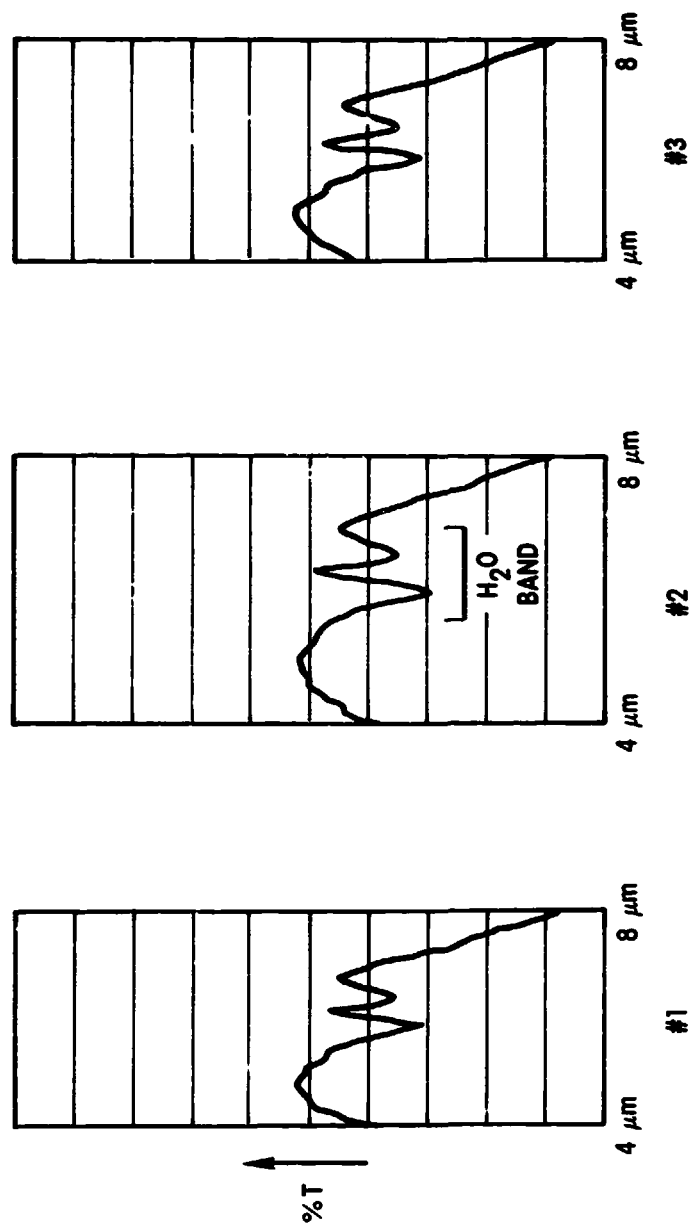


Fig. 11. Typical Background Spectra

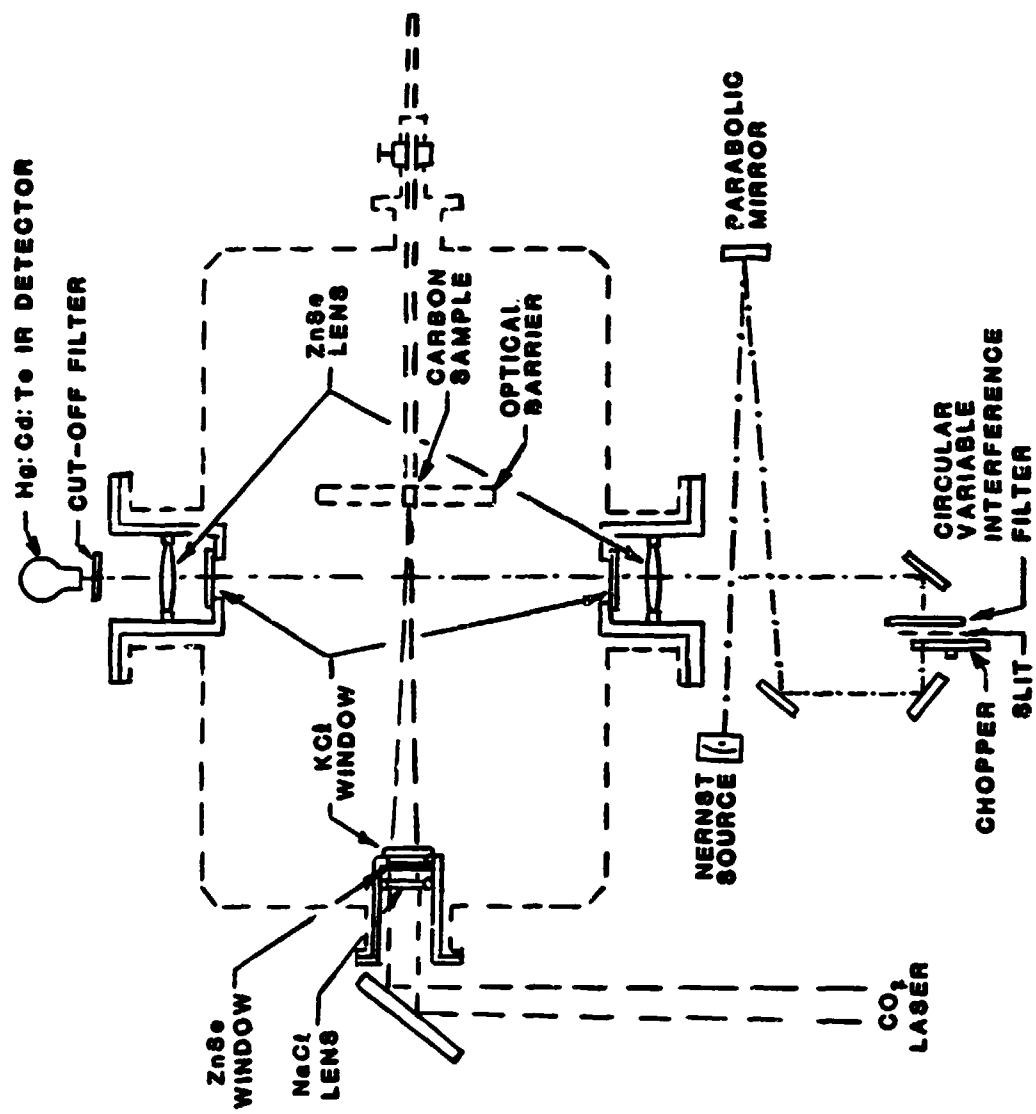


Fig. 12. Vacuum Chamber, Laser Transfer Optics, and Diagnostics

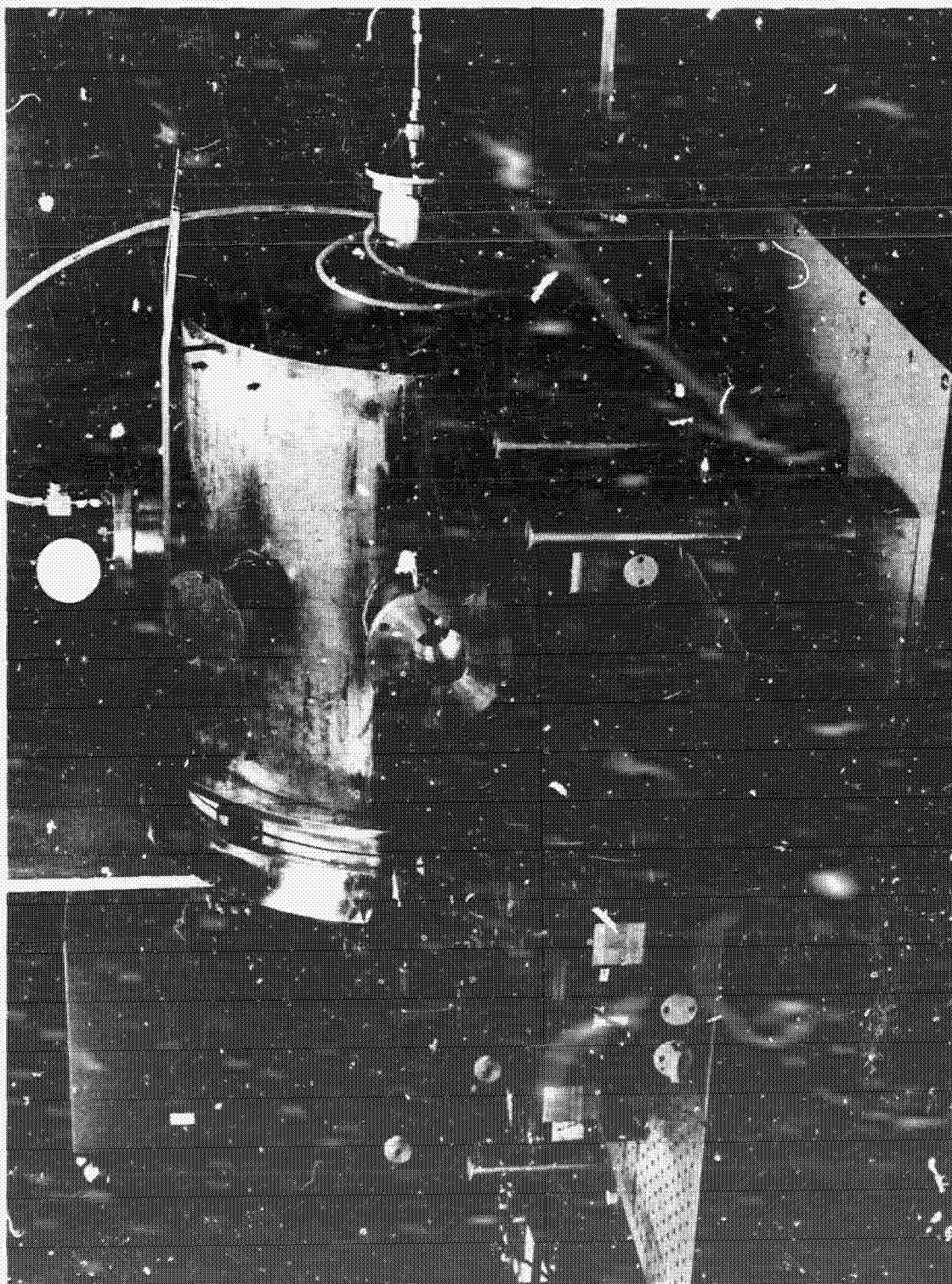


Fig. 13. Vacuum Chamber and Optical Bench

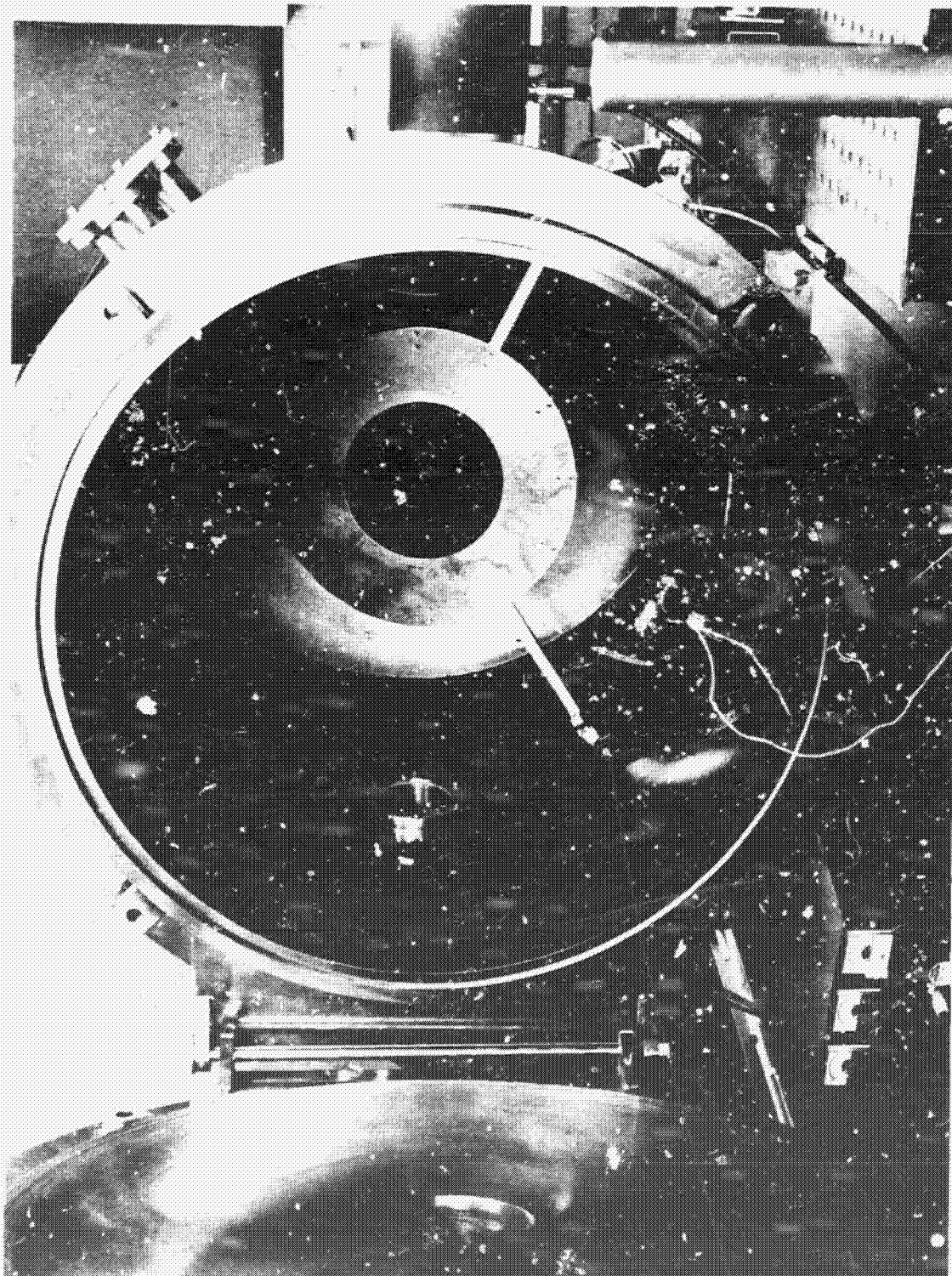


Fig. 14. Internal View of Vacuum Chamber

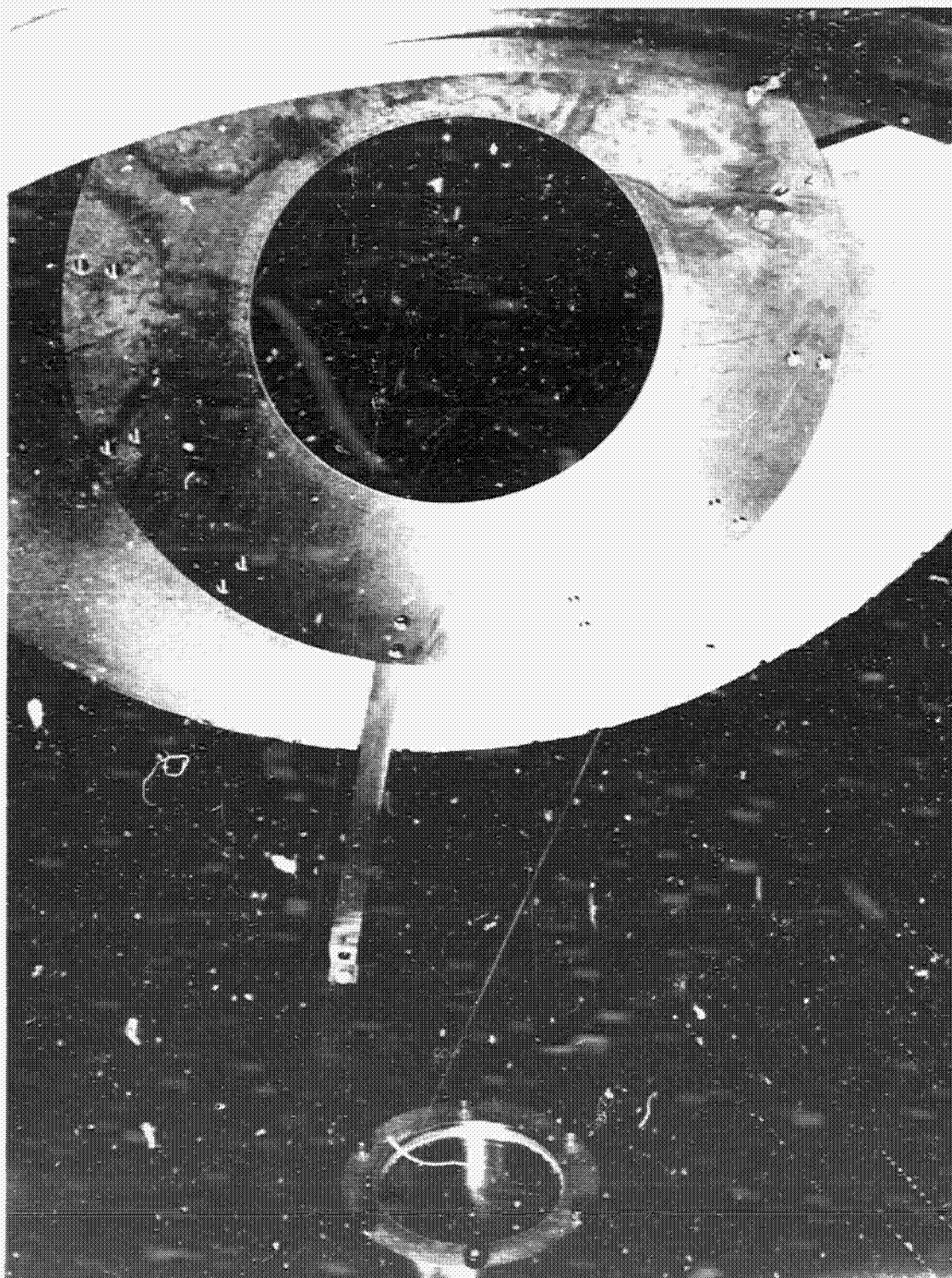


Fig. 15. Close-up View of Graphite Rod Sample
Mounted Along Chamber Axis

The CO₂ laser beam is introduced through a 6-in. diameter port located in the front door. The 6-in. diameter diagnostic ports are mounted in the chamber sides on a horizontal axis perpendicular to the laser optical axis. Additional instrumentation can be mounted at 4-in. diameter ports located at 45° to the horizontal axis and perpendicular to the laser optical axis. Test samples are introduced through a 4-in. diameter port in the rear of the chamber. This port contains a valve and seal such that the samples can be introduced with the chamber at reduced pressure.

Incident CO₂ laser radiation, not falling directly on the sample, is absorbed by a 7-in. diameter carbon plate. This carbon plate is mounted in a 12-in. diameter aluminum plate which is supported from the inner walls of the chamber by a spider.

The chamber can be evacuated by diffusion and backing pumps through a 6-in. diameter port in the bottom of the chamber. Dry nitrogen or inert gases can be introduced through an 8-in. diameter port located in the top of the chamber.

2. CO₂ Laser Transfer Optics

Tests were conducted using The Aerospace Corporation Materials Sciences Laboratory's 1-kW CO₂ laser which delivered a multi-mode 3-in. diameter beam at the facility. Alignment of the optical axis of the laser with the optical axis of the test chamber was accomplished through a periscope. The periscope mirrors were 8-in. diameter plate copper.

The laser beam was focused to a diameter of 13 mm at the test sample by a 4-in. diameter KCl lens of 12-in. focal length. Lens protection was accomplished by using a replaceable 3-in. diameter KCl window. Vacuum integrity was accomplished by O-ring sealing on an AR-coated ZnSe window 3 in. in diameter.

3. Diagnostics

The diagnostic optical schematic is shown in Fig. 12. A blackbody continuum was produced from a Nernst glow-rod heater (Optitron Model IRR-30) operating at approximately 2100°K. The source was focused onto a 25-mm x 2.5-mm slit, through a Rofin MK II Type 7500 light chopper by a 3-in. diameter, 10-in. focal length parabolic mirror. The wavelength region of 4-12 μm was scanned every 1.5 sec by a circular variable interference filter.

The resulting radiation was focused as a 12.5-mm x 1.2-mm slit-image at the center of the chamber by a 2-in. diameter, 8-in. focal length ZnSe lens. Radiation transmitted through the plume region was then focused onto a HgCdTe detector by a 2-in. diameter, 2-in. focal length ZnSe lens. The vacuum integrity as well as lens protection were accomplished by using replaceable 3-in. diameter KCl windows.

Data were processed through a Princeton HR-8 lock-in amplifier and Brush Mark 280 strip-chart recorder. A blocking filter with an 8- μm cutoff was used at the detector to prevent spectral-order overlap and to suppress scattered 10.6- μm laser radiation while testing occurred in the 4-8 μm region.

4. Operating Procedure

Each experiment was performed by installing a carbon rod, evacuating and refilling (if desired) the chamber, and then pre-focusing and aligning the 1-kw CO₂ laser using a coaligned He-Ne beam. The wavelength range was selected and the appropriate blocking filter was installed. The circular variable filter was rotated at approximately 0.7 rps. This typically provided a 0.75-sec 4-8 μm spectrum, followed by a filtered 7-12 μm spectrum. Thus, a useful spectrum was recorded every 1.5 sec. When 7-12 μm spectroscopy was selected, the 7-12 μm blocking filter acted to completely block the 4-8 μm data. The spectroscopy was recorded for a period of 5-10 sec before the high power laser was turned on; it was terminated when the post-burn spectrum resembled the pre-burn spectrum in peak transmission.

C. EXPERIMENTAL RESULTS

Our experimental approach was to use the limited time available with the 1-kW CO₂ laser facility to conduct a survey of the primary variables involved.

The following variables were investigated:

- o Infrared Wavelength Range. Two CVIFs were available for these initial experiments: a 4-8 μm filter and a 7-12 μm filter
- o Type of Carbon. Three carbons were vaporized: Graphnol, pyrolytic graphite (perpendicular to lamellar planes), and Poco-graphite
- o Probe Spatial Location. 1.5-sec spectroscopy across the plume was performed at three axial distances from the vaporizing carbon rod source: 6 mm, 18 mm, and 30 mm
- o Chamber Pressure. Experiments were conducted at pressures of 10^{-2} , 1, 30, 300, and 760 torr. Argon was used as the inert gas

A summary of the experimental matrix and result notations appears in Table 1.

1. First Experiments

Initial experiments were conducted using Graphnol rods in a near-vacuum (10^{-2} torr argon) environment and with the 4-8 μm CVIF placed at the chopper (see Fig. 12). Spectral scans were recorded from the slit probe-beam which passed perpendicular to the incoming 10.6 μm laser energy, approximately 18 mm (6 rod diameters) from the end of the rod. This geometry is shown pictorially shown in Fig. 15 and schematically in Fig. 16. As with most survey experiments, there are always surprises. Our very first experiment (22-1) produced results which we had not anticipated. When the CO₂ laser was turned on, delivering approximately 960 W onto the end of the 3-mm diameter rod, the 4-8 μm spectral signature was quickly almost totally

Table 1. Spectroscopy Runs

Run No.	Chamber Pressure (torr)	Material	Filter	x/d	Laser Power (W)	Comments	Signal Recovery After Laser-Off (sec)
22-1	10^{-2}	Graphnol	4-8 μ m @ chopper	6	960	10.6 μ m scattering, 10-15% attenuation after laser-off	3
23-1	10^{-2}	Graphnol	7-12 μ m @ chopper	6	980	10.6 μ m scattering, 10-15% attenuation after laser-off	10+
23-2	5×10^{-2}	Graphnol	7-12 μ m @ chopper	2	950	Strong scattering, 80% attenuation after laser-off	35+
24-1	5×10^{-2}	Graphnol	4-8 μ m @ detector	2	850	Low scatter, 50% attenuation during laser-on	30
24-2	10^{-1}	Graphnol	4-8 μ m @ detector	10	1000	Low scatter, 20% attenuation during laser-on	3-4
25-1	10^{-2}	Pyrolytic Graphite	4-8 μ m @ detector	2	900	Low scatter, 50% attenuation during laser-on	90
25-2	10^{-1}	Pyrolytic Graphite	4-8 μ m @ detector	10	925	Low scatter, 10% attenuation during laser-on	<1
26-1	5×10^{-2}	Poco	4-8 μ m @ detector	2	875	Low scatter, 80-90% attenuation during laser-on	50 - 60
26-2	10^{-2}	Poco	4-8 μ m @ detector	10	925	Low scatter, 20% attenuation during laser-on	12
27-1	1	Graphnol	4-8 μ m @ detector	10	850	Almost no modulation, 10-20% attenuation	2 - 3
27-2	30	Graphnol	4-8 μ m @ detector	10	900	Slight modulation, 10-20% attenuation	2 - 3
27-3	300	Graphnol	4-8 μ m @ detector	10	925	Moderate modulation, 10-20% attenuation	4 - 5
28-1	760	Graphnol	4-8 μ m @ detector	6	880	20-40% Absorption, lessens for $t > 3$ sec	3-4
28-2	760	Pyrolytic Graphite	4-8 μ m @ detector	6	980	Modulation (scattering), spectrum recovery at ~3 sec	3
29-1	760	Poco	4-8 μ m @ detector	6	975	Severe modulation (scattering), spectrum reappears $t > 3$ sec	6

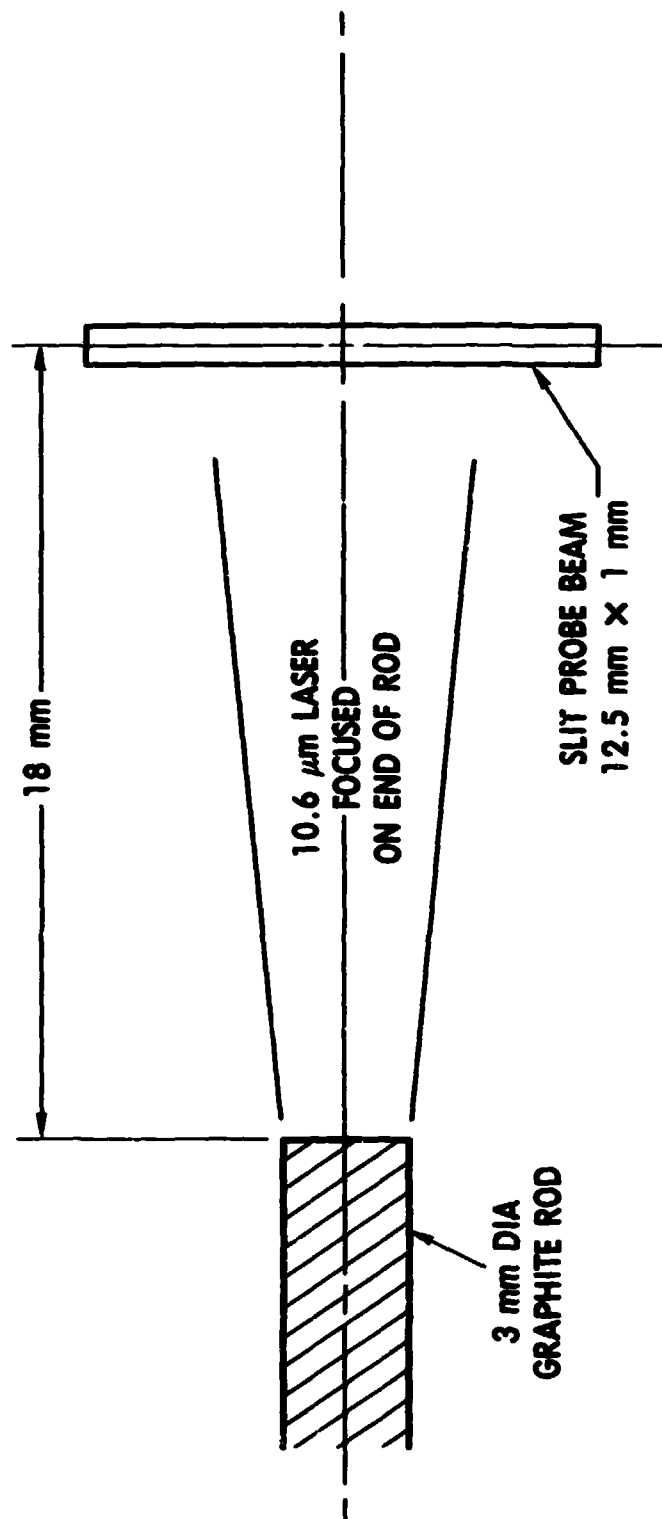


Fig. 16. Probe Beam Geometry

masked by particle-modulated 10.6 μm scattered light from the CO_2 laser. Unexpectedly, there were sufficient carbon particles near the end of the carbon rod source to produce the amount of spectral modulation that was observed. What had been anticipated was that carbon particle condensation would occur some distance from the carbon source. Based upon this assumption, we expected that there would be a condensation zone which would cover the range from gaseous carbon through small particles to a coalesced particle regime.

With our geometrically well-defined optical diagnostic capability, if a vapor zone had existed in this region, there would have been little attenuation of the transmitted spectrum and a low level of observed 10.6 μm scattered light. Our observations are presented in Fig. 17 which shows a typical pre-burn spectrum, a portion of the burn spectrum, and part the first post-burn spectrum which demonstrates the attenuation of the transmitted beam through the cooling plume.

From this first test result, we concluded that there were a substantial number of particulates 18 mm from the end of the carbon source. Also, the intensity of the scattered light was strong from the point of turn-on and remained fairly constant through the 4-sec burn sequence. In the first post-burn spectrum, where the 10.6- μm scattered radiation was no longer present, a 10 to 15 percent attenuation was observed at all wavelengths. Complete return to the pre-burn spectrum occurred in about 3 sec. The peak transmission points on each side of the atmospheric 6.25- μm water absorption correspond to 4.86 μm and 6.86 μm . Approximately 10 percent greater absorption was observed from the longer wavelength in the first post-burn spectrum.

A second experiment (23-1) was conducted under the same conditions, using the 7-12 μm CVIF. All the observations noted in the first experiment apply also to the results of this experiment, including the increased attenuation at longer wavelengths. In both experiments, there were no intense or easily identified molecular or structured absorption features in the post-burn spectra.

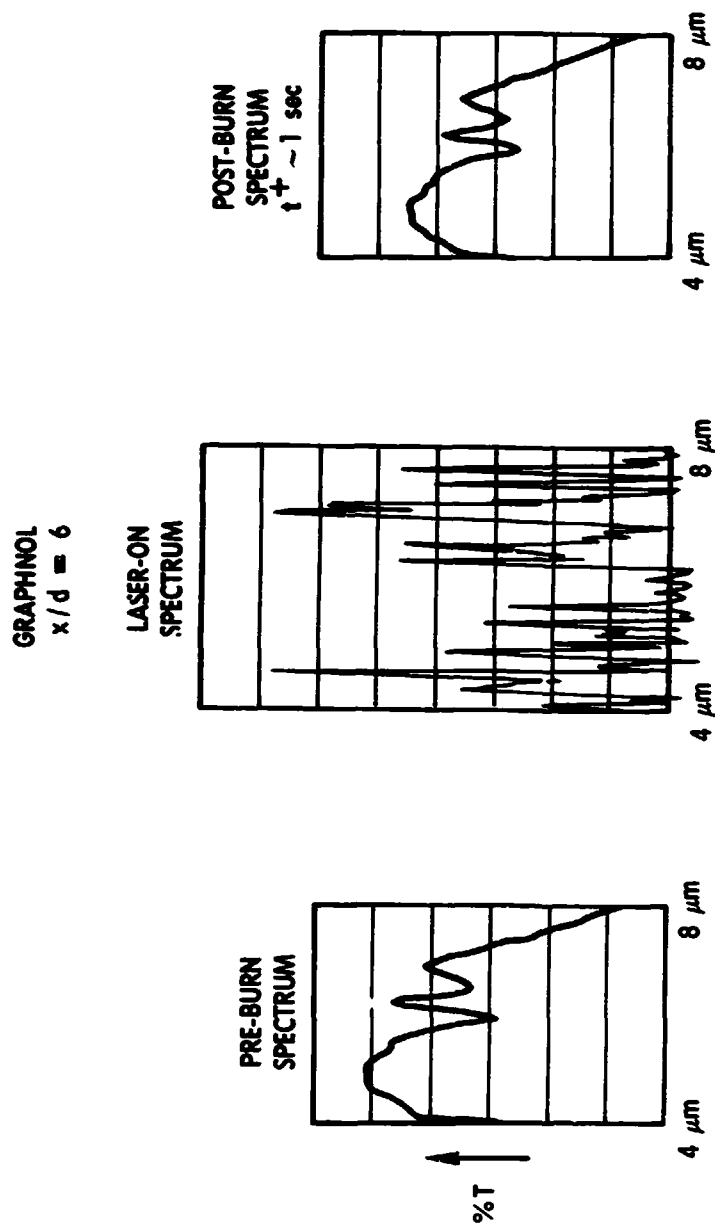


Fig. 17. 4-8 μ m Plume Spectroscopy (Run 22-1)

The last experiment in this initial series (23-2) was a repeat of 23-1 with diagnostics conducted 6 mm (compared with 18 mm) from the end of the carbon source. Representative 7-12 μm spectral scans from this run are shown in Fig. 18. It was expected that there would be fewer particles at this distance and therefore less absorption and less scattering of the 10.6 μm CO_2 laser energy.

The exact opposite was observed. There was greater attenuation of the diagnostic beam--approximately 80 percent for the first post-burn spectral scan. The intensity of the modulated 10.6- μm light was 50 percent greater. Again, there was stronger attenuation at long wavelengths. Measured attenuation ratios were 1.72 between 7 and 12 μm . This number compares well with a ratio of 1.71 if the attenuation is proportional to wavelength. Surprisingly, the recovery to the pre-burn transmission conditions required over 35 sec indicating that particulates were either continuing to be generated after the CO_2 laser was shut off or required long settling times to clear the field of view.

On the assumption that vacuum plume streamlines near the end of the vaporizing carbon rod "loft" small particles which settle when the laser is turned off, settling times were calculated based upon both continuum and collisionless gas dynamics. Details of the calculations are given in Appendix B. The conclusion is that if the long post-burn spectral recovery times are caused by the slow settling of lofted particles, then the particles are exceedingly small (10-30 nm).

After the results of the first three tests were assessed, a new experimental strategy was developed. It was decided that our best chance of reducing the scattered 10.6 μm light and performing spectroscopy during the burn phase would be to perform 4-8 μm spectroscopy on the remaining experiments. The 4-8 μm blocking filter, which highly attenuates 10.6 μm light, was moved to a position directly in front of the detector. Using this strategy, we completed a series of 12 additional experiments to study different types of graphite with near and far field diagnostics at ambient pressures ranging from 10^{-2} to 760 torr (see Table 1). These experiments are described in the following subsections.

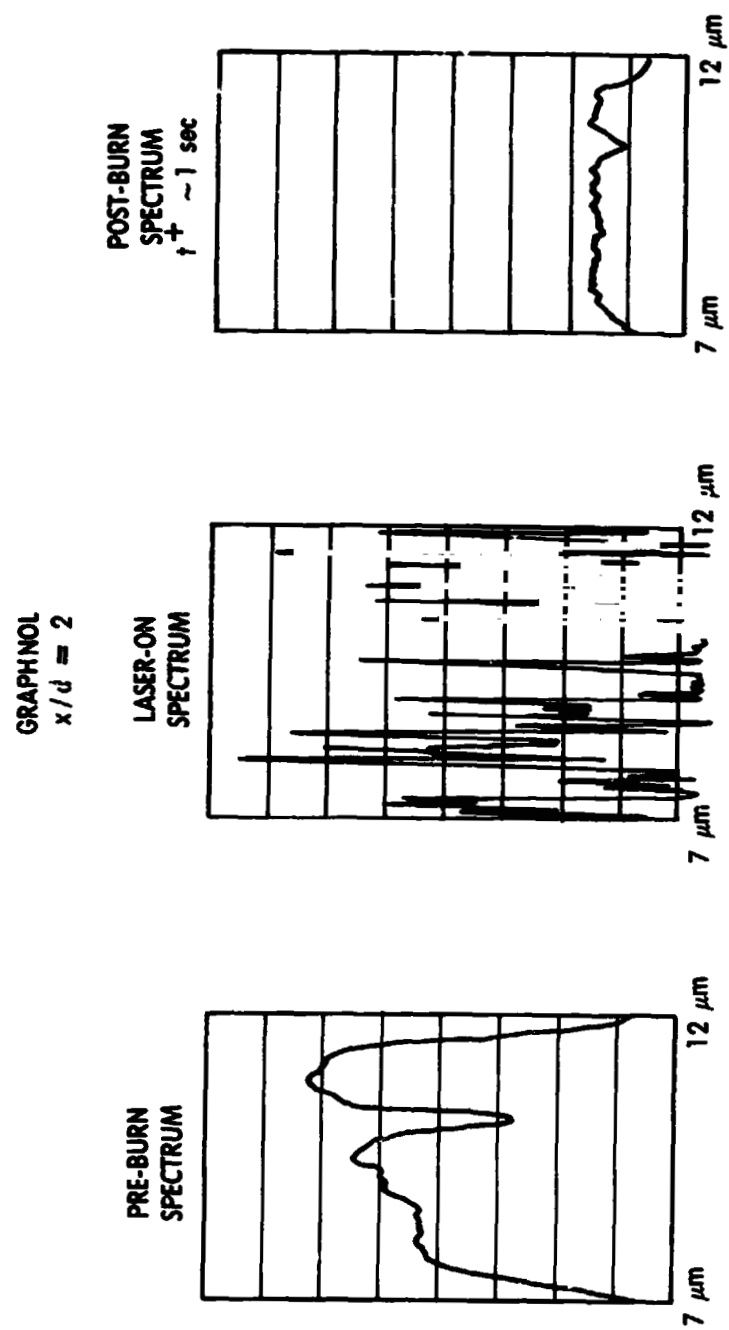


Fig. 18. 7-12 μm Plume Spectroscopy (Run 23-2)

2. Effect of Varying Graphite Material and Probe Axial Location

In this series, six experiments (24-1 through 26-2) were conducted at near-vacuum chamber conditions. Three graphites--Graphnol N3M¹⁰, pyrolytic graphite (Super Temp, continuously nucleated), and Poco (AXF.Q1)--were studied at diagnostic probe points 6 and 30 mm from the end of the carbon rod. The results are partly predictable and otherwise interesting. The 10.6 μm scattered radiation problem was substantially reduced, allowing 4-8 μm spectral scans to be seen during the laser-on time. The data for the two diagnostic probe distances confirmed our earlier conclusion; namely, that greater numbers of particles are found closer to the end of the plume source. Also, as in the initial experiments, the post-burn spectral recovery period is much longer during probing close to the rod, i.e., 3-12 sec at a distance of 30 mm and 30-90 sec at 6 mm. The percentage of probe energy attenuation is 5 to 20 percent at 30 mm; at 6 mm from the end of the rod, as much as 80 to 90 percent attenuation was observed.

In many ways, the three types of graphite tested gave similar results. Absorption and scattering of infrared radiation by particles was observed for all three materials. At an axial station of 30 mm (10 rod diameters), the fractional absorption (up to 20 percent) was essentially independent of material type (see Fig. 19). This figure also illustrates that during the run, the level of modulated 10.6- μm light is least for Graphnol and greatest for pyrolytic graphite.

At 6 mm (see Fig. 20), much greater absorption of the probe energy occurred. All three graphites showed an increased particle density build-up with time. The build-up was fastest for pyrolytic graphite because of its low thermal conductivity along the rod axis and the resulting much shorter time (10.1 sec) to steady-state ablation. The greatest absorption during laser-on (90 percent) occurred with the Poco-graphite.

$$x/d = 10$$

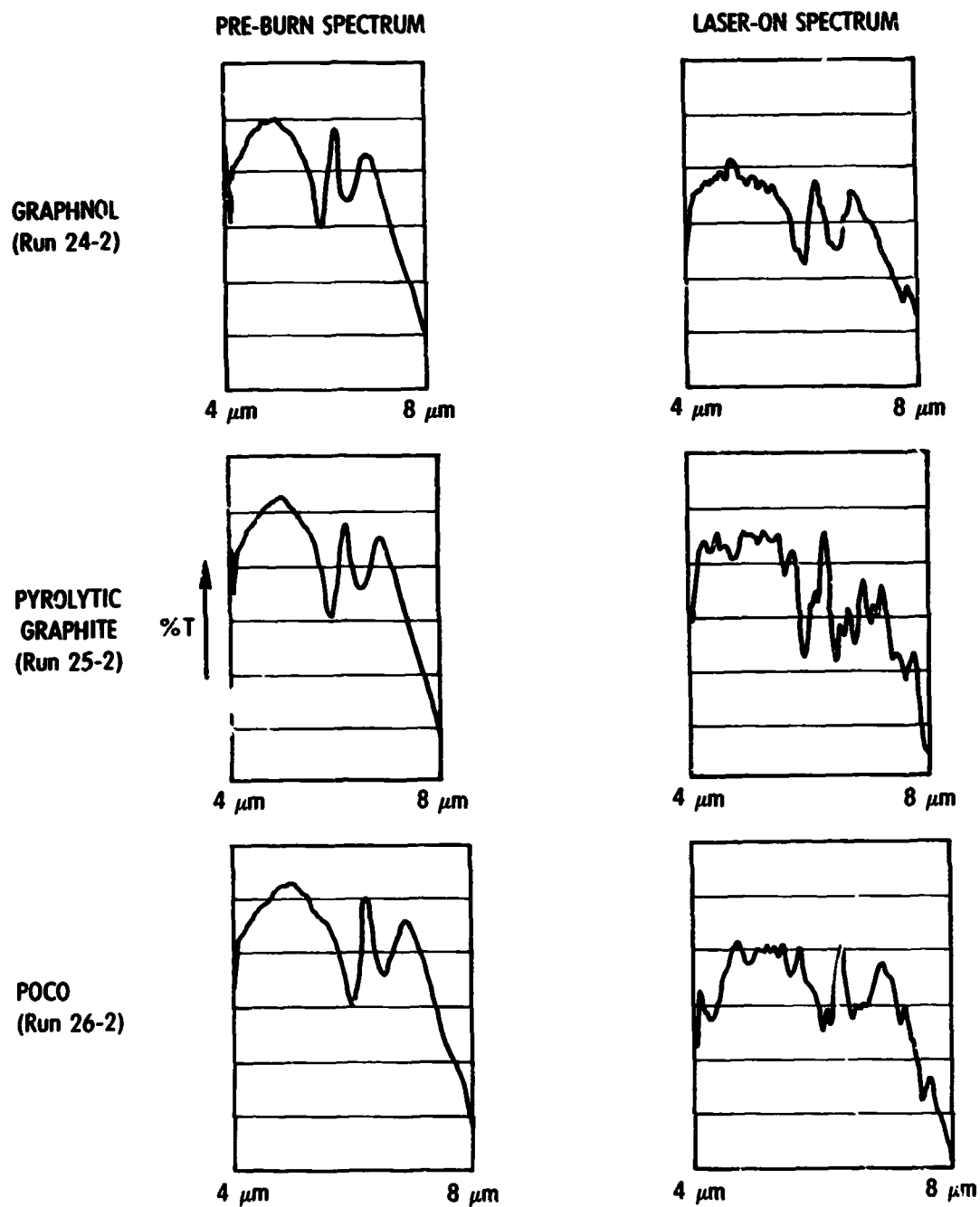


Fig. 19. Laser-on Spectroscopy

$$x/d = 2$$

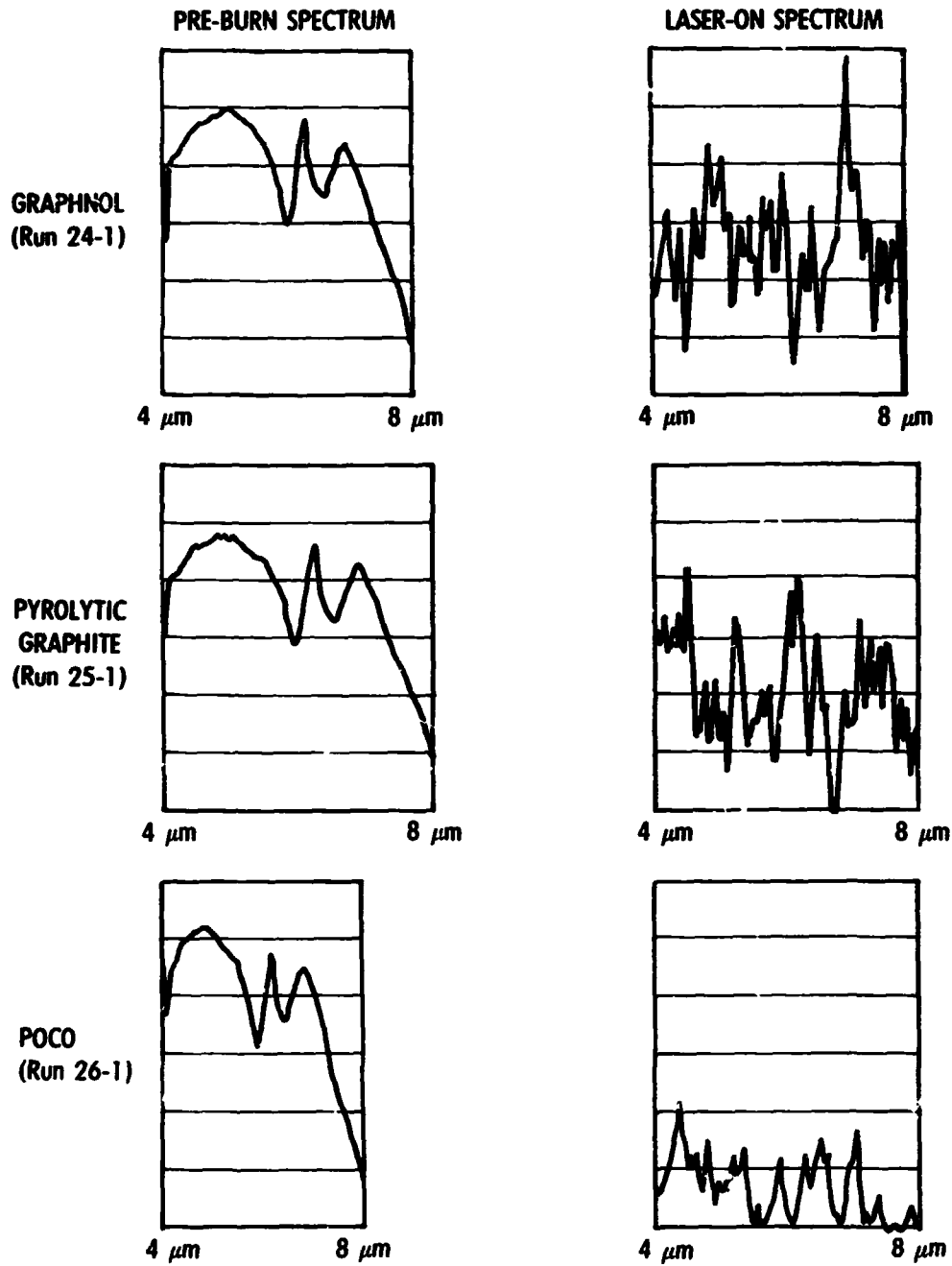


Fig. 20. Laser-on Spectroscopy Close to End of Rod

Post-burn spectral signal recovery times were approximately 30, 60, and 90 sec for Graphnol, Poco, and pyrolytic graphite, respectively. The slow signal recoveries can be seen in the first three post-burn spectral scans for these materials shown in Fig. 21. We note, cautiously, that all three graphites indicate the presence of an absorption band at $7.4 \mu\text{m}$ (1350 cm^{-1}) in the immediate post-burn spectra. There has been no attempt to assign this feature to a molecular species.

Overall, these experiments indicate that more particulates (absorption) were generated with the Poco graphite than with the other two graphites. However, the modulated $10.6\text{-}\mu\text{m}$ light (scattering) was greatest for the pyrolytic graphite.

3. Effect of Finite Ambient Pressures

A series of three experiments (27-1,2,3) was run with Graphnol rods at argon pressures of 1, 30, and 300 torr. A diagnostic distance of 30 mm was chosen, since an increase in particulate concentration was anticipated due to the higher pressures and mixing of the hot carbon vapors with the cold ambient gas.

Once again, the results of these tests did not confirm our expectations. Attenuation of the probe beam was approximately 20 percent during the laser-on time and was essentially independent of pressure. However, modulation of the $10.6\text{-}\mu\text{m}$ light was 3.5 times larger at 300 torr than at 1 torr. These effects are illustrated in Fig. 22. There were indications that the $7.4\text{-}\mu\text{m}$ band was again present and particularly strong in some of the laser-on spectra. There may also be a spectral feature at $5 \mu\text{m}$ which correlates with the $7.4\text{-}\mu\text{m}$ band intensity. The triatomic carbon molecule, C_3 , has a rotation/vibration band near $5 \mu\text{m}$.¹⁷ Spectral recovery times were on the order of 3 to 5 sec.

A final series of three experiments (28-1, 28-2, 29-1), using all three graphites, was carried out with an ambient pressure of 760 torr in argon. The $4\text{-}8 \mu\text{m}$ spectroscopy was performed 6 mm from the end of the carbon source.

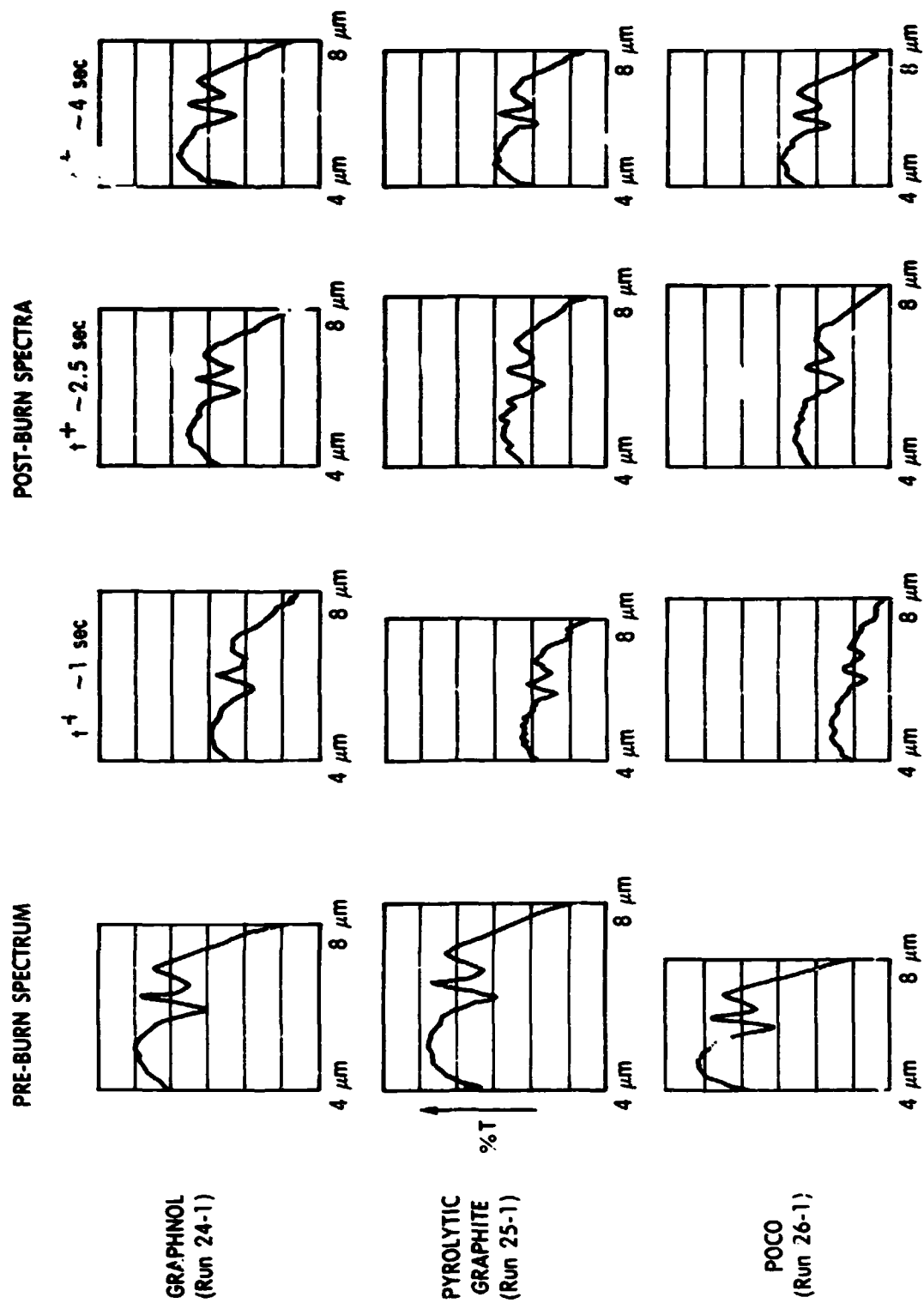


Fig. 21. Probe Beam Transmission Recovery Effects

GRAPHINOL
 $x/d \approx 10$

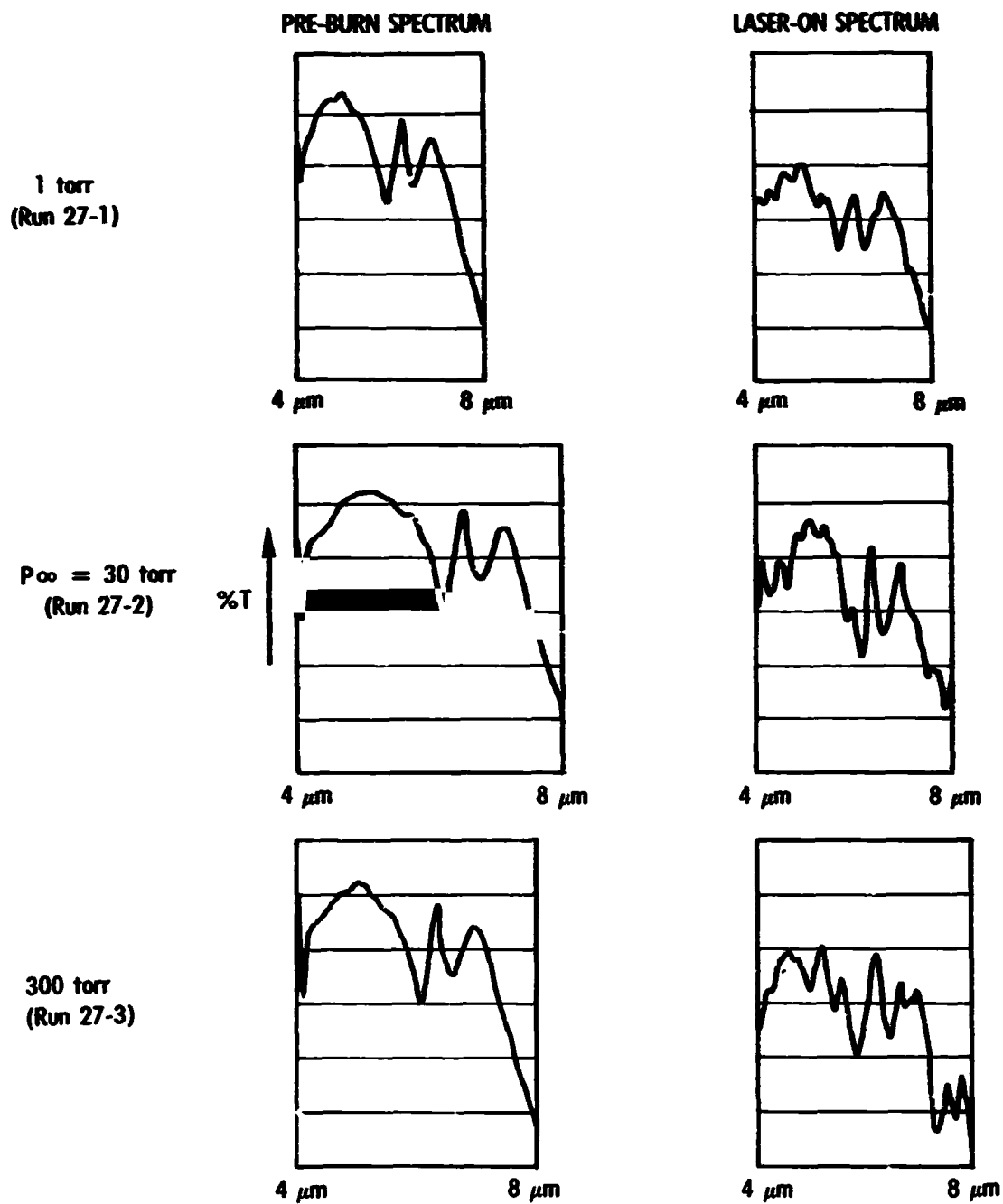


Fig. 22. Spectra at Various Chamber Pressure

This series showed interesting results. First, the Graphnol produced the least amount of modulation of 10.6 μm radiation. The attenuation increases with time for about 3 sec and then decreases. Poco-graphite produced the greatest 10.6 μm modulation. However, after about 3 sec of burn, the modulation decreased and the spectrum began to reappear. Maximum attenuation in the post-burn spectra appeared to be 20 to 30 percent. Pyrolytic graphite showed a similar effect with a spectrum reappearing approximately 2 sec into the burn. These effects are shown in Fig. 23.

These tests apparently indicate that about halfway into the burn, all the graphites produced sufficient particulate densities to initiate blockage of the incoming CO_2 laser energy. Many large-scale (0.1-1 mm) "fluffy" particles of carbon condensate were observed in the chamber after each of these runs. Some of these were collected for later analysis. The post-test appearance of the samples (Fig. 24) indicates that the major source of these large pieces may have been condensation and subsequent detachment from the end of the vaporizing (subliming) carbon rod during the run. Graphite rods exposed to laser radiation at lower ambient chamber pressures did not exhibit this phenomenon.

D. OBSERVATIONS

At least three unexpected results were produced from this series of experiments:

- o Attenuation of the probe beam by the plume increased as the beam was positioned closer to the end of the carbon rod.
- o Transmission measurements through the plume showed preferentially increased attenuation at longer wavelengths.
- o Extremely long (up to 90 sec) probe beam attenuation recovery times were observed after laser turn-off.

Understanding these results is an important goal, since they appear to be related to each other and should reveal a great deal about the fundamental processes involved.

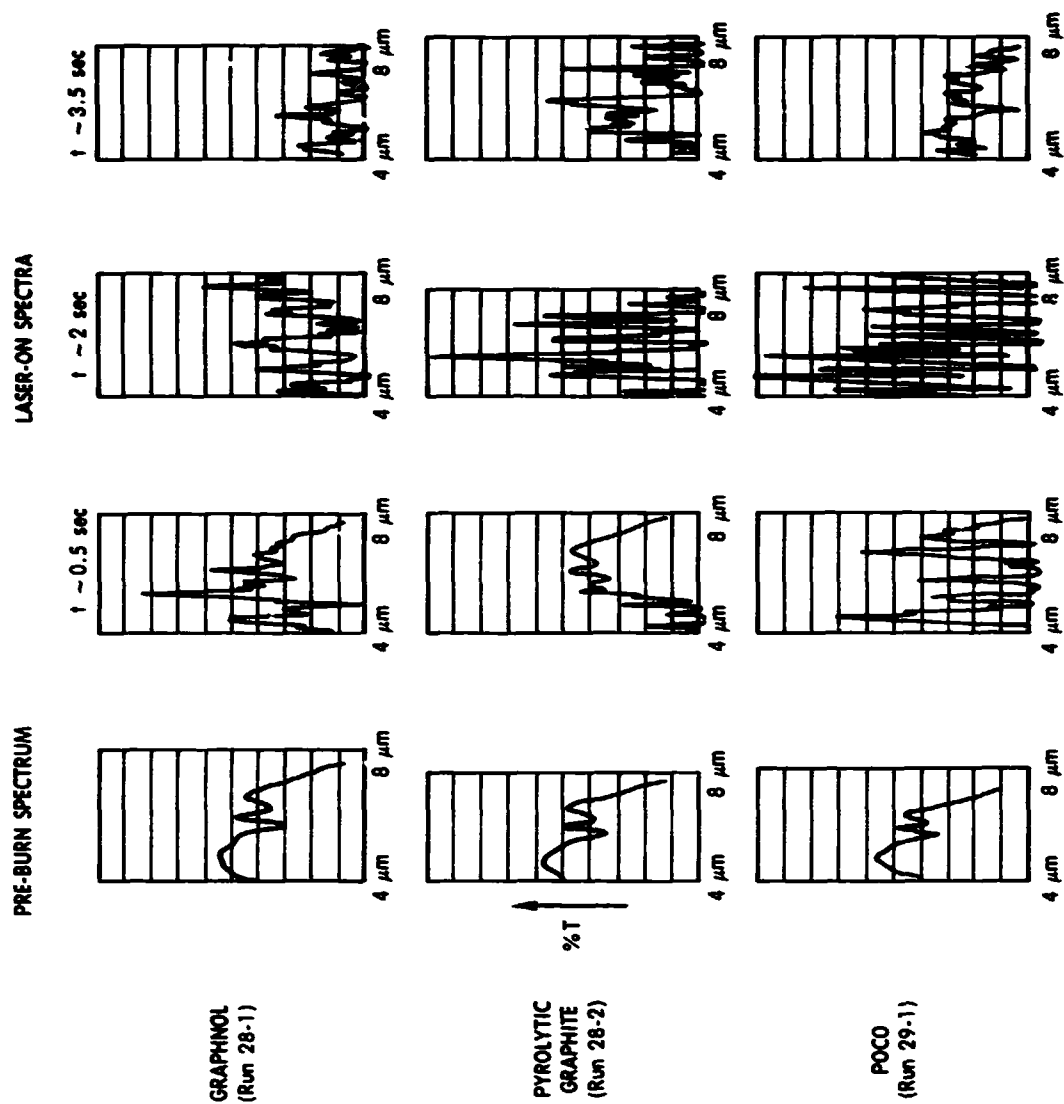


Fig. 23. 4-8 μm Spectroscopy, Chamber Pressure = 1 atm, $x/d = 6$



Fig. 24. Post-test Appearance of Graphnol Rod (16X)

Stronger attenuation of the probe beam, when it was positioned closer to the end of the carbon rod, can only be interpreted as more particles per cm^2 . Thus, the data indicate that if a condensation zone exists, it is within the 6mm minimum distance studied in our experiments. The reason for this is depicted qualitatively in Fig. 25. The upper figure, 25a, shows the behavior of the driving force for condensation processes (i.e., the supersaturation ratio) as a function of distance from the end of the rod. Figure 25b illustrates the behavior of the collision frequency of molecules within the plume. Since the number of condensed particles present at any time depends on the product of these two quantities, the particle density reaches a maximum value and then decreases due to volumetric dilution (Fig. 25c). If condensation is occurring in our experiments, the peak particle density is very close to the end of the rod.

A very reasonable and likely alternative explanation of what we are seeing is that the particles are being emitted^{18,19} from the vaporizing carbon surface. In this instance, we would expect to see the attenuation continue to increase as the probe beam approaches the end of the rod. This is shown schematically by the dashed line in Fig. 25c. More detailed probing with greater resolution near the end of the vaporizing rod, some carefully planned experiments, and particle collection will be required to finally resolve the question of particle origins.

The observed increased attenuation with wavelength and the long signal recovery times after laser-off are both connected in some way with particle sizes. Our calculations of particle sizes, based upon the assumption that they are "lofted" within the chamber (Appendix B), indicate particle sizes the order of 0.001 times the wavelength of the probe light. In this regime, we

¹⁸Whittaker, A. G. and P. L. Kintner, "Particle Emission and Related Morphological Changes Occurring During the Sublimation of Graphitic Carbons," Carbon, Vol. 14, 1976, pp. 257-265.

¹⁹Abrahamson, J., "Graphite Sublimation Temperatures, Carbon Arcs, and Crystallite Erosion," Carbon, Vol. 12, 1974, pp. 111-141.

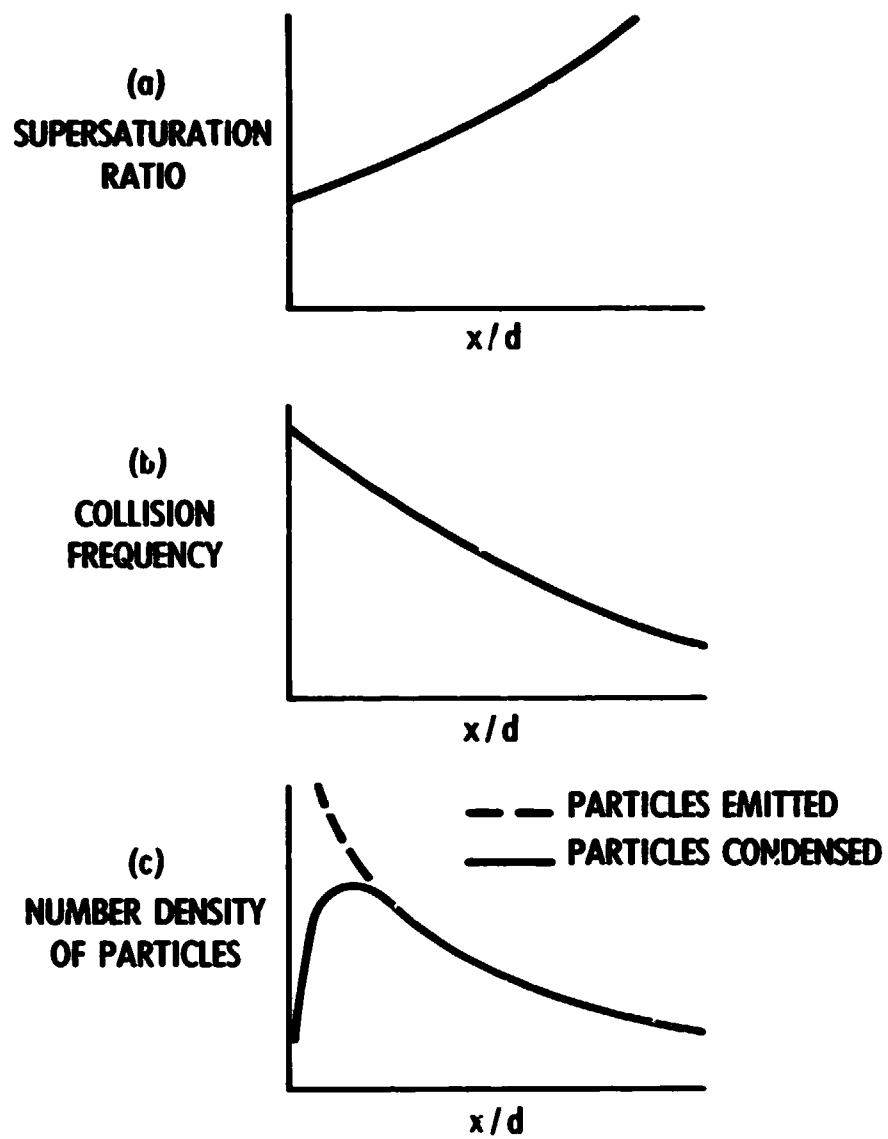


Fig. 25. Axial Distribution of Condensation Factors and Particles

would expect to see absorption scale inversely with wavelength²⁰ rather than directly with wavelength as observed experimentally. However, if the particles were slightly larger than the wavelength scanned, the observed wavelength dependence might be explainable in terms of the Mie theory.²¹ Production of large particles is consistent with the physical properties of the graphites used. Representative grain sizes for Poco graphite, Graphnol, and pyrolytic graphite are the order of 3 μ m, 30 μ m, and 300 μ m, respectively.*

Finally, we note an unresolved discrepancy in the above discussion. If the particles are large so as to possibly explain the attenuation behavior with wavelength, they will quickly fall to the bottom of the chamber after laser-off. However, very small particles are required to explain the long signal recovery times. Alternative explanations are needed.

We plan to resolve these questions in the near future by carrying out additional experiments using the hardware and diagnostic methods now available. The primary objectives of new work would be to:

- o Identify the particle-generating mechanism (emitted, condensed, or both)
- o Collect and characterize particles over a wide range of ablating surface temperatures
- o Relate observed particle effects (i.e., absorption/scattering) to the solid-state properties of the type of carbon vaporized and to the properties of collected particles
- o Further investigate possible molecular absorption features seen near 5 μ m (likely triatomic carbon, C₃) and 7.4 μ m
- o Extend our diagnostics to cover the entire 2.5-14 μ m mid-IR spectral range

²⁰Hottel, H. C. and A. F. Sarofin, Radiative Transfer, McGraw-Hill Book Co., N.Y., 1967, Chapter 12, 13.

²¹Van der Hulst, H. C., Light Scattering by Small Particles, Dover Publications, Inc., NY (1981).

* Chase, A.B., Personal communication, The Aerospace Corporation, El Segundo, CA.

V. SUMMARY AND CONCLUSIONS

The overall objectives of our four years of work have been to gain a better understanding of the superior energy-dissipating efficiency of carbon materials and to determine the limits of their outstanding thermal protection system performance. The method used to accomplish this goal has been to develop analytical techniques which allow detailed analyses of nonequilibrium carbon laser ablation experiments. Our analytical approach, data analysis conclusions, and their relevance, are summarized below.

In order to relate experimentally measured quantities, such as mass loss rates and surface temperatures, to desired thermochemical properties, we developed a multispecies nonlinear model of nonequilibrium carbon ablation under laser irradiation. The initial model was based upon solving the species mass, momentum, and energy conservation equations across the nonequilibrium region (Knudsen layer) at the surface. The importance of ad hoc closure methods associated with the conservation equation approach was investigated by using higher order methods (Boltzmann equation and Molecular Dynamics) to solve for the changes in macroscopic variables across the Knudsen layer. These methods established the validity of the more approximate conservation equation solutions which were used for our data analyses. We have also now established a hierarchy of models which can be applied to other complex and theoretically difficult physical/chemical problems.

Using the above model as a data analysis tool, we find that our continuous wave (CW) and pulsed laser ablation experiments have indicated the following:

- o The vapor pressure of carbon is best represented by the Lawrence Livermore Laboratory thermochemical properties.^{12,13}
- o The melt temperature of carbon is in the range of 4500-4800°K
- o Vaporization coefficients, which define the kinetic rates of carbon vaporization, are strongly temperature-dependent. The vaporization coefficients for Graphnol and for pyrolytic graphite (when vaporization takes place perpendicular to the planes) are about the same. When pyrolytic graphite vaporization occurs parallel to the planes, the vaporization coefficients are approximately a factor of three higher.

- o The high temperature ablated-surface emissivities of Graphnol and pyrolytic graphite (viewed parallel to the planes) are near unity. For pyrolytic graphite viewed perpendicular to the planes, the high temperature ablated-surface emissivity is estimated from our data to be 0.85.

Our analytical model, together with the above carbon properties data, allows reliable thermal protection system design calculations to be made for the projected use of carbon materials in very severe heating and nonequilibrium ablation environments. The most serious limitations to ultimate performance capability appear to be: degradation of mechanical properties at temperatures above 4000°K, rapidly increasing surface recession rates which increase from 25 mm/sec (1 in/sec) to 300 mm/sec (1 ft/sec) as the temperature rises from 4200 to 4500°K, and melting above 4500°K. To reach 4500°K, a local heat flux of about 2 MW/cm^2 ($1,760,000 \text{ Btu/ft}^2\text{-sec}$) is required.

In addition to the above basic studies, a preliminary investigation of particle effects in a laser-vaporized carbon plume has been completed using spectroscopic methods. From these initial experiments, the following observations have been made:

- o Severe particulates blockage (80 to 90 percent) of probe-radiation from an infrared source occurs when one views through the laser-vaporized carbon vapor plume at a location close (6 mm) to the vaporizing surface ($p = 10^{-2}$ torr).
- o The absorption increases with wavelength and, in some instances, is proportional to wavelength.
- o When probes are made at locations farther from the source (18 mm, 30 mm), the blockage is much less.
- o During the laser heating time, the spectroscopic signature is strongly modulated by $10.6 \mu\text{m}$ laser radiation scattered by particles in the plume.
- o The likely source of the particles is particulate emission from the ablating surface. Condensation in the highly supersaturated carbon vapor remains as a possible alternate or simultaneous particle generating source.

- o Although quantitative comparisons are difficult, Poco graphite appears to produce more particles (and greater infrared radiation blockage) than Graphnol or pyrolytic graphite.
- o Our present experiments and analysis give inconsistent conclusions regarding particle sizes.
- o At higher chamber pressures, especially at 1 atm, more particles and greater laser radiation blockage were observed.

REFERENCES

1. Baker, R. L., "Carbon Nonequilibrium Phase Change," Office of Naval Research Interim Report, TR-0081(6728-02)-1, The Aerospace Corporation, El Segundo, CA, Dec. 1981.
2. Baker, R. L. and M. A. Covington, "The High Temperature Thermochemical Properties of Carbon," Office of Naval Research Interim Report, TR-0082(2729)-1, The Aerospace Corporation, El Segundo, CA, Mar. 1982.
3. Baker, R. L., M. A. Covington, and G. M. Rosenblatt, "The Determination of Carbon Thermochemical Properties by Laser Vaporization," High Temperature Materials Chemistry Symposium, The Electrochemical Society, 1983, pp. 143-154.
4. Baker, R. L., M. A. Covington, and K. A. Lincoln, "The Vapor Pressure, Melt Temperature and Vaporization Kinetics of Carbon," J. Appl. Phys., (To be published).
5. Turner, J. S., "Laser-Induced Phase Changes at Solid Surfaces," Final Report, The University of Texas at Austin, October 1982.
6. Baker, R. L., D. A. Nelson, and J. S. Turner, "Higher Order Numerical Simulations of the Knudsen Layer," Office of Naval Research Interim Report, TR-0083(3729)-2, The Aerospace Corporation, El Segundo, CA, Apr. 1983.
7. Touloukian, Y. S., ed., Thermophysical Properties of Matter, Vol. 8, IFI/Plenum Press, NY, 1970.
8. Pyrolytic Graphite Handbook, Metallurgical Production Department, General Electric Company, Schenectady, NY, 1964, as quoted in Gokcen, N.A., et al., "Determination of Graphite/Liquid/Vapor Triple Point by Laser Heating," High Temperature Science, Vol. 8, June 1976, pp. 81-97.
9. Brookley, C.E., "Product Data for High Temperature Pyrometers," Thermogage, Inc., Frostburg, MD, 1982. Also, "Calibration Curves for the Aerospace High Temperature Pyrometer."
10. Johnsen, B. P. and H. S. Starrett, "Preliminary Design Data Package for Graphnol N3M (Phase III, Mantech)," Report SORI-MEK-82-20, Southern Research Institute, Birmingham, AL, Nov. 1982.
11. JANAF Thermochemical Tables, National Bureau of Standards, NBS-37, June 1971.
12. Lee, E. L. and R. H. Sanborn, "Extended and Improved Thermal Functions for the Gaseous Carbon Species C₁-C₇ from 298 to 10,000°K," High Temperature Science, Vol. 5, 1973, pp. 438-453.
13. Leider, H. R., O. H. Krikorian, and D. A. Young, "Thermodynamic Properties of Carbon Up to the Critical Point," Carbon, Vol. 11, 1973, pp. 555-563.

REFERENCES (Continued)

14. Rosenblatt, G. M., "The Role of Defects in Vaporization: Arsenic and Antimony," Surface Defect Properties of Solids, Vol. 5, 1976 pp. 36-64.
15. Rosenblatt, G. M., "Evaporation from Solids," Treatise on Solid State Chemistry, Vol. 6a, N. B. Hannay (ed.), Plenum Press, NY, 1976, p. 199.
16. Hirth, J. P. and G. M. Pound, "Condensation and Evaporation," Progress in Materials Science, Vol. 11, MacMillan Publishing Co., Inc., NY, 1963.
17. Treffers, R. R. and D. P. Gilra, "The Vibrational Spectrum of C₃ in the 5 Micron Region," Astrophysical J., Vol. 202, 1975, pp. 839-843.
18. Whittaker, A. G. and P. L. Kintner, "Particle Emission and Related Morphological Changes Occurring During the Sublimation of Graphitic Carbons," Carbon, Vol. 14, 1976, pp. 257-265.
19. Abrahamson, J., "Graphite Sublimation Temperatures, Carbon Arcs, and Crystallite Erosion," Carbon, Vol. 12, 1974, pp. 111-141.
20. Hottel, H. C. and A. F. Sarofin, Radiative Transfer, McGraw-Hill Book Co., NY, 1967, Chapters 12, 13.
21. Van der Hulst, H. C., Light Scattering by Small Particles, Dover Publications, Inc., NY, 1981.
22. Bird, G. A., Molecular Gas Dynamics, Oxford University Press, London, 1976.

INDEX OF TECHNICAL REPORTS

1. "Carbon Nonequilibrium Phase Change," Interim Report, TR-0081(6728-02)-1, The Aerospace Corporation, El Segundo, CA, Dec. 1981.
2. "The High Temperature Thermochemical Properties of Carbon," Interim Report, TR-0082(2729)-1, The Aerospace Corporation, El Segundo, CA, Mar. 1982.
3. "Higher Order Numerical Simulations of the Knudsen Layer," Interim Report, TR-0083(3729)-1, The Aerospace Corporation, El Segundo, CA, Apr. 1983.
4. "Carbon Vaporization/Condensation Effects," Final Report, TR-0084(9990)-1, The Aerospace Corporation, El Segundo, CA, March 1984.

INDEX OF PUBLICATIONS

1. "A Steady-State Melt Layer Model with Absorption, Conduction and Surface Evaporation," Lett. Heat and Mass Trans., Vol. 9, 1982, pp. 299-308.
2. "The Near-Surface Nonequilibrium Gas Dynamics of Laser Vaporized Materials," AIAA J., (To be published).
3. "The Determination of Carbon Thermochemical Properties by Laser Vaporization," High Temperature Materials Chemistry Symposium, The Electrochemical Society (1983), pp. 243-254.
4. "The Vapor Pressure, Melt Temperature, and Vaporization Kinetics of Carbon," J. Appl. Phys., (To be published).

APPENDIX A

ONE-DIMENSIONAL STEADY-STATE ABLATION OF A SLENDER ROD

The components of the steady-state energy balance for laser irradiation of an absorbing solid material target are shown in Fig. A-1. In order to gain a complete understanding of the energy dissipation efficiency of a particular material, one must predict and experimentally measure each of these components. In many instances, the conduction of energy into the solid, q_{cond} , does not achieve a steady-state (constant) value during the time that the material is irradiated by the laser. This complicates the analysis process by requiring that predicted quantities and experimental data must both be determined as functions of time.

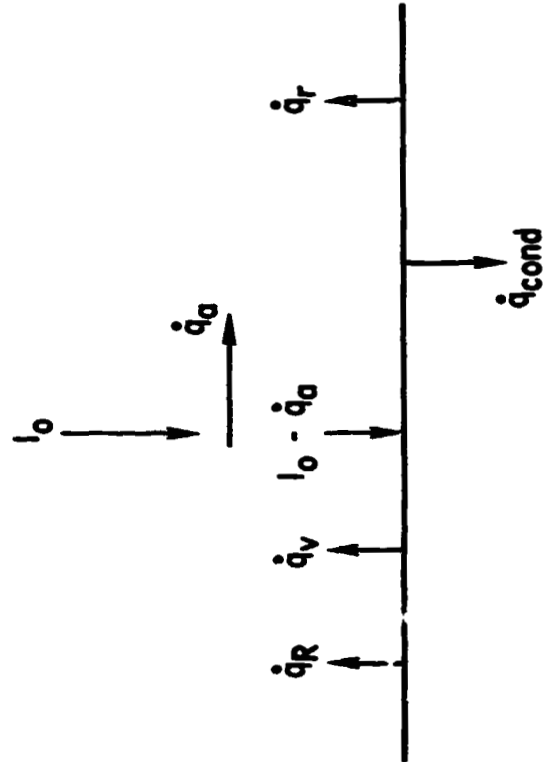
Often the transient heating time is lengthened by radial conduction of energy away from a small laser-irradiated spot on the surface. In such instances, accurate analysis is further complicated by the laser-ablated hole which forms in the solid and which may alter the expansion of vaporized material away from the surface. A slender rod sample-geometry for laser irradiation experiments eliminates radial conduction and hole-boring effects. The end of the rod is "flood-loaded" by the incoming laser energy, and a steady-state ablation rate and temperature distribution are rapidly established.

The purpose of this appendix is to describe the differential equation and boundary conditions governing this problem, to show numerically obtained representative solution behavior, and to briefly discuss two applications of this type of solution.

A-1. DIFFERENTIAL EQUATION AND BOUNDARY CONDITIONS

The heat conduction equation describing energy transport for a one-dimensional steady-state ablation process was first derived by

I_o — INCOMING RADIATION FLUX
 \dot{q}_a — EFFECTIVE RADIATION ABSORPTION
 \dot{q}_R — REFLECTED RADIATION FLUX
 \dot{q}_v — ENERGY FLUX DUE TO MASS TRANSPORT
 $I_o - \dot{q}_a$ — ATTENUATED FLUX REACHING SURFACE
 \dot{q}_{cond} — ENERGY FLUX INTO MATERIAL AS HEAT
 \dot{q}_r — EMITTED RADIATION FLUX FROM SURFACE



$$I_o - \dot{q}_a - \dot{q}_R - \dot{q}_v - \dot{q}_{cond} - \dot{q}_r = 0$$

Fig. A-1. Energy Partitioning at Surface

Landau.¹⁶ For stationary surface recession velocity \dot{s} , and distance x measured from the moving surface, the governing differential equation is

$$\frac{d^2 \bar{T}}{dx^2} + \frac{\dot{s}}{\alpha_T} \frac{d\bar{T}}{dx} = 0 \quad (\text{A-1})$$

where α_T is the thermal diffusivity and T is the temperature. Landau presented solutions to this equation with appropriate boundary conditions. In Ref. 12, Landau's solution was extended to include a melted layer of absorbing and conducting liquid above the solid.

For a slender cylindrical rod, the one-dimensional heat conduction equation when similarly transformed becomes

$$\frac{d^2 \bar{T}}{dx^2} + \frac{\dot{s}}{\alpha_T} \frac{d\bar{T}}{dx} = \frac{4\sigma\epsilon \bar{T}^4}{kD} \quad (\text{A-2})$$

where

k = thermal conductivity

D = rod diameter

ϵ = emissivity of rod surface

σ = Stefan-Boltzmann constant for radiative heat transfer

The term on the right-hand side of Eq. (A-3) arises due to radiative loss of energy from the cylindrical surface of the rod.

When we non-dimensionalize by the end-surface temperature T_s and the thickness of the thermal layer δ , it is convenient to define new variables T and x by

$$T = \frac{\bar{T}}{\bar{T}_s}, \quad x = \frac{\bar{x}}{\delta} \quad (\text{A-3})$$

Equation (A-3) now becomes

$$\frac{d^2 T}{dx^2} + \left(\frac{\delta}{\alpha_T} \frac{dT}{dx} \right) = \left\{ \frac{4\sigma\epsilon\bar{T}_o^4}{kD\bar{T}_s/\delta^2} \right\} T^4 \quad (A-4)$$

subject to the boundary conditions

$$T(0) = 1, \quad T(1) = T_\infty \quad (A-5)$$

Because the thickness of the thermal layer δ appears directly in the differential equation, a further condition is needed to define δ . A global energy balance provides the required constraining equation, i.e.

$$\left\{ \frac{kD\bar{T}_s/\delta^2}{4\sigma\epsilon\bar{T}_s^4} \right\} \left(\frac{dT}{dx} \right)_{x=0} = \int_0^1 T^4 dx + \left\{ \frac{\rho s C_p \bar{T}_s}{4\sigma\epsilon\bar{T}_s^4} \right\} \frac{D}{\delta} (1 - T_\infty) \quad (A-6)$$

The term on the left in Eq. (A-6) is the energy conducted into the rod at the end. This energy is dissipated in two ways. The integral term on the right represents the total energy radiated from the cylindrical surface of the rod. The last term on the right-hand side is the energy required to heat the rod from temperature \bar{T}_∞ to \bar{T}_s , assuming that C_p is not a function of temperature.

A-2. NUMERICAL SOLUTION PROCEDURE

Equation (A-4) is a nonlinear two-point boundary value problem with boundary conditions [Eq. (A-5)]. In the present analysis it was solved using standard second order accurate centered differencing after the application of quasilinearization to obtain a linear approximation. For any fixed $\delta > 0$, the iterations associated with the quasilinearization converge fairly rapidly. Iteration tolerances of 10^{-4} were employed with a max-norm convergence criterion. Typically, between two and six iterations were needed.

The grid spacing, h , used in most runs was $h = 0.02$. A few runs were made with $h = 0.01$ and $h = 0.005$ to verify grid function convergence. It was found that the $h = 0.02$ results were within a few percent of converged solutions.

The energy balance, Eq. (A-6), provides the equation for determining δ . This expression is highly nonlinear with respect to δ , because T and dT/dx are implicitly functions of δ through Eq. (A-4), in addition to the explicit quadratic dependence shown in Eq. (A-6). Equation (A-6) was solved by Newton's method, but with numerical approximations of derivatives with respect to δ used for terms for which analytical derivatives could not be calculated (the terms containing T and dT/dx). Because of the need for such approximations, and also because of the high degree of nonlinearity, convergence was sometimes slow. Nevertheless, complete solutions to the system consisting of Eqs. (A-4), (A-5), and (A-6) could always be obtained within approximately 20 iterations of Eq. (A-6).

The overall computational algorithm consists of the following steps:

- a. Guess a value of δ and a temperature distribution, $T(x)$.
- b. Solve Eq. (A-4) with boundary conditions (A-5) (Note that the quasilinear iterations should be carried to convergence.).
- c. Perform a single Newton iteration step on Eq. (A-6) to obtain an improved value of δ .
- d. Test convergence of δ . If δ is converged, stop. Otherwise, repeat steps 2 and 3.

A-3. REPRESENTATIVE SOLUTIONS

Anticipating the use of calculated solutions in conjunction with the experiments described in Section V of this report, we selected a nominal rod diameter D of 3mm (9.84×10^{-3} ft). The values of heat capacity C_p and thermal conductivity k used for initial calculations were

$$C_p = 0.543 \text{ Btu/lb-}^\circ\text{R}$$

$$k = 0.00295 \text{ Btu/ft-sec-}^\circ\text{R}$$

These values are representative of graphite at high temperatures. In order to minimize the time required to calculate solutions, the surface recession rate \dot{s} (ft/sec) was represented as a function of surface temperature T_s by the function

$$\dot{s} = Ae^{-E/RT_s}$$

where $A = 7.69 \times 10^9$ and $E/R = 187,207$ $^\circ\text{R}$ for T_s in $^\circ\text{R}$. This expression was obtained from carbon nonequilibrium ablation calculations discussed in Refs. 13-15.

From the calculated steady-state temperature distributions in the rod, the heat conducted into the rod \dot{q}_c and the thermal layer thickness δ were determined. Representative values of \dot{q}_c and δ for surface emissivities of 0.5-1.0 at increments of 0.1 and for surface temperatures of 5400 $^\circ\text{R}$ (3000 $^\circ\text{K}$), 6000 $^\circ\text{R}$ (3323 $^\circ\text{K}$), 6600 $^\circ\text{R}$ (3667 $^\circ$) and 7200 $^\circ\text{R}$ (4000 $^\circ\text{K}$) are shown in Table A-1.

For the lowest surface temperature, the surface recession rate \dot{s} is essentially zero. In this case, the solution represents a steady state energy balance in which laser energy is conducted along the rod and radiated out the side. For the highest surface temperature, the surface recession rate \dot{s} is 11.97 mm/sec (4.71 in./sec). In this instance, considerable laser energy is accommodated by the ablation process, and the remaining energy is conducted

Table A-1. Dependence of Calculated Results on Surface Emissivity and Temperature

$d=d_o = 0.00984 \text{ ft}$			
T (°R)	ϵ	δ (ft)	Btu/ft ² sec \dot{q}_c
5400	1.0	0.185781	1012.876
	0.9	0.194788	960.385
	0.8	0.205389	904.922
	0.7	0.218107	845.907
	0.6	0.233724	782.528
	0.5	0.253395	713.587
6000	1.0	0.168189	1343.513
	0.9	0.177473	1275.782
	0.8	0.188365	1204.191
	0.7	0.201642	1127.959
	0.6	0.218171	1046.062
	0.5	0.239578	957.011
6600	1.0	0.250717	2276.801
	0.9	0.268295	2203.255
	0.8	0.289088	2126.875
	0.7	0.314296	2047.339
	0.6	0.345518	1964.284
	0.5	0.385383	1877.251
7200	1.0	0.111267	16137.18
	0.9	0.112002	16121.95
	0.8	0.112747	16106.71
	0.7	0.113502	16091.46
	0.6	0.114268	16076.21
	0.5	0.115044	16060.95

into the rod and again radiated out the side. We note that when \dot{s} is high, δ and \dot{q}_c are insensitive to the emissivity ϵ ; whereas when \dot{s} approaches zero, δ increases and \dot{q}_c decreases as ϵ decreases, for a given surface temperature T_s . The sensitivity of calculated solutions to the rod diameter and the thermal conductivity is shown in Tables A-2 and A-3, respectively. Results are again shown for the same surface temperatures as in Table A-1. To a rough approximation, except for $T_s = 7200^\circ\text{R}$, the dependence on rod diameter and thermal conductivity is represented by

$$\begin{aligned} \text{(effect of rod diameter)} \quad \delta &\rightarrow \left(\frac{d}{d_o}\right)^{1/2}, & \dot{q}_c &\rightarrow \left(\frac{d}{d_o}\right)^{-1/2} \\ \text{(effect of conductivity)} \quad \delta &\rightarrow \left(\frac{k}{k_o}\right)^{1/2}, & \dot{q}_c &\rightarrow \left(\frac{k}{k_o}\right)^{1/2} \end{aligned}$$

where d_o and k_o are the nominal values used for the calculated results given in Table A-1. For $T_s = 7200^\circ\text{R}$, δ and \dot{q}_c are relatively insensitive to diameter; \dot{q}_c increases slightly as k increases, however, δ is nearly directly proportional to k , varying by a factor of 70 when k increases two orders of magnitude.

A-4. APPLICATIONS

The application of these solutions to data analysis is straightforward and direct. Unfortunately, we were not able to obtain measured surface temperatures on the ablating end of the rod during the test series described in Section V of this report. For low laser energy input levels, we believe that these solutions can be used to determine the emissivity ϵ of the graphite rod. For the higher laser input energies, this solution method provides a tool which can be readily used to evaluate each term (see Fig. A-1) in the energy balance equation for steady-state ablation. From this, the contribution of each dissipation mechanism to the overall ablation efficiency can be determined for various materials of interest.

Table A-2. Sensitivity to Rod Diameter

$\epsilon = 0.9$			
T	d/d_o	δ	\dot{q}_c
5400	0.1	0.064249	3054.506
	1	0.194788	960.385
	2	0.284471	681.461
	3	0.347652	556.364
	10	0.634412	304.924
6000	0.1	0.056490	3997.324
	1	0.177473	1275.782
	2	0.253511	909.671
	3	0.312051	746.761
	10	0.601726	419.500
6600	0.1	0.057084	3515.368
	1	0.268295	2203.255
	2	0.410115	1831.997
	3	0.514038	1688.795
	10	0.872119	1465.880
7200	0.1	0.074029	17339.88
	1	0.112002	16121.95
	2	0.115529	16052.46
	3	0.116719	16029.60
	10	0.118440	15997.44

Table A-3. Sensitivity to Thermal Conductivity

T	k/k_o	δ	\dot{q}_c	T	k/k_o	δ	\dot{q}_c
5400	0.1	0.063939	305.535	6600	0.1	0.087279	1465.801
	1	0.194788	960.385		1	0.268295	2203.255
	10	0.633841	3043.923		10	0.561721	5496.961
6000	0.1	0.062899	423.384	7200	0.1	0.011900	15992.44
	1	0.177473	1275.782		1	0.112002	16121.95
	10	0.555039	3979.489		10	0.741124	17338.61

APPENDIX B

PARTICLE SIZES DERIVED FROM SETTLING TIMES

If it is assumed that the long probe-beam recovery times seen experimentally are associated with particles "lofted" in the chamber at the probe station, then approximate particle sizes can be obtained by comparing predicted settling times with those seen in the data. Alternatively, the settling time t , the settling velocity V_s , and the settling length L_s are related by $V_s = L_s/t$. When $L_s = 1$ ft (half the chamber diameter) is used for the settling length, the observed long settling times of 30 to 90 sec, give V_s values from 0.011 to 0.033 ft/sec. The purpose of this appendix is to determine for what range of particles sizes the predicted velocities are in the observed range. Calculations based upon the bounding cases of continuum and collisionless gas dynamics were carried out.

B-1. PARTICLE SIZES PREDICTED FROM CONTINUUM GAS DYNAMICS

For a particle settling in a fluid, the terminal velocity is determined by a balance of the acceleration force F_g due to gravity and the retarding force F_v due to viscous forces. For a particle of radius R and density ρ , F_g is the product of the volume, density, and acceleration due to gravity, i.e., $F_g = (4/3\pi R^3)\rho g$. The drag force F_v for viscous-dominated Stokes flow is $F_v = 6\pi\mu R V_\infty$ where μ is the viscosity of the fluid and V_∞ is the velocity of the particle through the fluid.

Equating these two forces and solving for the velocity V_∞ , we obtain

$$V_\infty = \frac{2\rho g R^2}{3\mu} \quad (B-1)$$

For particles of given density in a fluid of known viscosity, V_∞ depends only upon R^2 . This relationship is shown by the heavy solid line in Fig. (B-1).

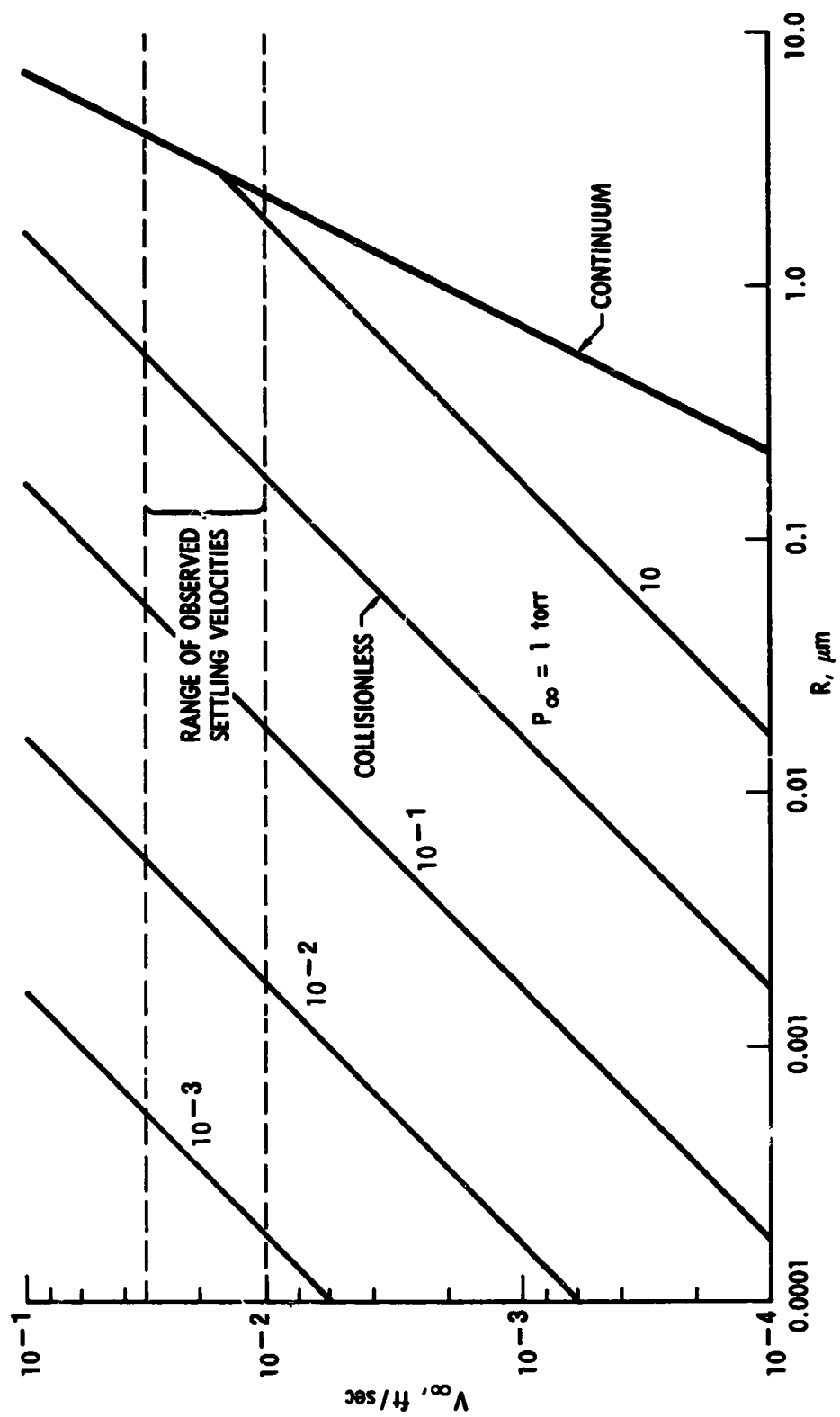


Fig. B-1. Relationship of Particle Size to Settling Velocity

B-2. PARTICLE SIZES PREDICTED FROM COLLISIONLESS GAS DYNAMICS

For this case, the drag coefficient $C_D = F_D / 1/2 \rho_\infty V_\infty^2 R^2$ is given by²²

$$C_D = \frac{2S^2 + 1}{\pi^{1/2} S^3} e^{-S^2} + \frac{4S^4 + 4S^2 - 1}{2S^4} \operatorname{erf}(S) + \frac{2(1-\xi) \pi^{1/2}}{3S} \left(\frac{T_w}{T_\infty} \right)^{1/2}$$

where the speed ratio S is given in terms of V_∞ and the gas constant R and temperature T_∞ by $S = V_\infty / \sqrt{2RT_\infty}$. In the last term, T_w is the particle temperature and ξ is the fraction of molecular collisions with particles that are specular rather than diffuse. In the following, we assume $T_w = T_\infty$ and $\xi = 0$.

For the settling velocity case in which we are interested, $V_\infty \ll \sqrt{2RT_\infty}$, i.e., S is small. When we substitute asymptotic expressions, valid for small S , in place of e^{-S^2} and the error function $\operatorname{erf}(S)$, we may combine the above expressions to obtain*

$$F_D = \frac{16}{3} \left[\frac{\pi m}{2kT_\infty} \right]^{1/2} \left[1 + \frac{\pi}{8} \right] p_\infty V_\infty R^2$$

Equating this force with the gravity force $F_g = (4/3 \pi R^3) \rho g$ and solving for V_∞ we obtain

$$V_\infty = \frac{\left[\frac{2\pi kT_\infty}{m} \right]^{1/2} g p R}{\left[4 + \frac{\pi}{2} \right] p_\infty} \quad (\text{B-2})$$

Comparing this with Eq. (B-1), we see that for the collisionless case the dependence on R is linear and V_∞ depends inversely on the ambient pressure p_∞ . For a room temperature ambient, Eq. (B-2) becomes

*Nelson, D. A., Personal Communication, The Aerospace Corporation, El Segundo, CA.

$$V_{\infty} = 0.0591 \frac{R}{p_{\infty}} \quad (B-3)$$

for V_{∞} in ft/sec, R in μm , and p_{∞} in torr. Representative results calculated using Eq. (B-3) are shown by the lighter lines in Fig. (B-1).

Thus, we conclude that for the range of settling velocities seen in our experiments, i.e., 0.011 to 0.033 ft/sec, the predicted particle sizes are

2-4 μm (for continuum flow)

8-20 nm (for collisionless flow, $p_{\infty} = 5 \times 10^{-2}$ torr)

For $p_{\infty} = 5 \times 10^{-2}$ torr, the mean free path for molecules is approximately 1000 μm , i.e., 1 mm. Since this is much larger than the predicted continuum particle sizes of 2-4 μm , the calculated particle sizes (continuum) are not likely to be correct, because the flow is not continuum. Conversely, the particle sizes predicted by the collisionless equations may be somewhat too small.